JOURNAL OF GEOPHYSICAL RESEARCH, VOL. 104, NO. C9, PAGES 20,617–20,637, SEPTEMBER 15, 1999

Boussinesq modeling of a rip current system

Qin Chen, Robert A. Dalrymple, James T. Kirby,
Andrew B. Kennedy, and Merrick C. Haller
Center for Applied Coastal Research, University of Delaware, Newark

Abstract. In this study, we use a time domain numerical model based on the fully nonlinear extended Boussinesq equations [*Wei et al.*, 1995] to investigate surface wave transformation and breaking-induced nearshore circulation. The energy dissipation due to wave breaking is modeled by introducing an eddy viscosity term into the momentum equations, with the viscosity strongly localized on the front face of the breaking waves. Wave run-up on the beach is simulated using a moving shoreline technique. We employ quasi fourth-order finite difference schemes to solve the governing equations. Satisfactory agreement is found between the numerical results and the laboratory measurements of *Haller et al.* [1997], including wave height, mean water level, and longshore and cross-shore velocity components. The model results reveal the temporal and spatial variability of the wave-induced nearshore circulation, and the instability of the rip current in agreement with the physical experiment. Insights into the vorticity associated with the rip current and wave diffraction by underlying vortices are obtained.

1. Introduction

Modeling surf zone hydrodynamics, including transformation of surface waves, cross-shore and longshore currents, and low-frequency motions, is of great interest for many reasons. Recently, advances have been made in extending the Boussinesq equations from a set of equations valid only for surface waves with very small wave numbers to numerical models that are now capable of modeling wave propagation from deep water to shallow water [see, e.g., *Madsen and Sørensen*, 1992; *Nwogu*, 1993; *Wei et al.*, 1995]. Wave breaking in surf zones is also incorporated into Boussinesq models by *Karambas and Koutitas* [1992], *Schäffer et al.* [1993], *Madsen et al.* [1997], *Svendsen et al.* [1996], and *Kennedy et al.* [1999], among others. On the other hand, advances in computer technology now permit the use of Boussinesq models for large nearshore regions and allow the averaging of model results to predict mean flows in the nearshore, including longshore and rip currents. The wave blockage by strong opposing currents is also simulated by *Chen et al.* [1998], using a Boussinesq model for the fully coupled wave and current motion. Literature reviews on recent advances in Boussinesq modeling of nearshore surface gravity waves are given by *Kirby* [1997] and *Madsen and Schäffer* [1999].

The concept of radiation stress introduced by *Longuet-Higgins and Stewart* [1961] and the pioneering work on longshore currents by *Bowen* [1969] and *Longuet-Higgins* [1970a, b], among others, form the theoretical foundation for understanding nearshore circulation generated by wave breaking. A recent literature review on surf zone hydrodynamics was made by *Svendsen and Putrevu* [1995]. In the literature, most of the numerical models for wave-induced nearshore circulation are based on the depth-integrated, time-averaged (over a short wave period) conservation laws of mass and momentum. Radiation stresses due to the short wave motion are taken as a forcing in the momentum equations for the mean flow, and the time-averaged mass flux of the short wave motion is included in the mass equation for the nearshore circulation. The effect of the underlying current field on the wave transformation can be taken into account by an iterative process [see, e.g., *Birkemeier and Dalrymple*, 1975], but it is time consuming in practice. The omission of wave-current interaction, however, can not be justified in the case of strong currents.

In this study, we employ a time domain numerical model based on the fully nonlinear Boussinesq equations introduced by *Wei et al.* [1995] to investigate the fully coupled interaction of surface waves with rip currents and the nearshore circulation generated by wave breaking on a barred beach with a rip channel. In section 2, we present the governing equations including additional terms to account for wave breaking, subgrid turbulent mixing, bottom friction, and shoreline run-up. Section 3 describes the numerical simulation of wave-induced nearshore circulation on a bar/trough beach with a rip channel. We present the spatial and temporal variation of the computed wave field, the underlying current field averaged over two wave periods, and the vorticity field obtained from both the averaged velocity field

Paper number 1999JC900154.
0148-0227/99/1999JC900154$09.00

and the instantaneous velocity of the combined wave and current motion. The numerical results are compared with laboratory measurements, including wave height, mean water level, and longshore and cross-shore currents along several transects. In section 4, an ideal bathymetry is introduced to study the effects of bathymetric nonuniformity on rip stability and vortex structure associated with the rip current. Comparison with the same set of laboratory data is presented. Section 5 is devoted to the study of wave refraction/diffraction by a rip current. Results from both the Boussinesq model and the refraction/diffraction (REF/DIF) model based on the parabolic approximation of the mild-slope equation show a similar diffraction pattern of the surface wave field by the underlying rip current. The implication of the diffracted wave field with respect to the nearshore circulation is discussed. Finally, we summarize the findings in section 6.

2. Model Formulation

2.1. Governing Equations

The extended Boussinesq equations of *Wei et al.* [1995] are written in terms of the velocity vector $\mathbf{u}_\alpha = (u_\alpha, v_\alpha)$ at a reference elevation z_α in the water column and the free surface elevation η relative to the still water level. The equation for conservation of mass may be written as

$$\beta\eta_t + \nabla\cdot\mathbf{M} = 0 \tag{1}$$

where

$$\mathbf{M} = \Lambda(h_0+\eta)\left\{\mathbf{u}_\alpha + \left[\frac{{z_\alpha}^2}{2} - \frac{1}{6}(h^2 - h\eta + \eta^2)\right]\nabla(\nabla\cdot\mathbf{u}_\alpha) + \left[z_\alpha + \frac{1}{2}(h-\eta)\right]\nabla[\nabla\cdot(h\mathbf{u}_\alpha)]\right\} \tag{2}$$

in which h is the still water depth, h_0 is the still water depth at the offshore limit of the slot, the subscript t denotes time differentiation, and ∇ is the horizontal gradient operator. In addition, β and Λ are two dimensionless multipliers introduced for the treatment of shoreline run-up as described in section 2.2. The associated momentum conservation equation is

$$\mathbf{u}_{\alpha t} + (\mathbf{u}_\alpha\cdot\nabla)\mathbf{u}_\alpha + g\nabla\eta + \mathbf{V}_1 + \mathbf{V}_2 - \mathbf{R}_b - \mathbf{R}_s + \mathbf{R}_f = 0 \tag{3}$$

where g is the gravitational acceleration and $\mathbf{V}_1$ and $\mathbf{V}_2$ are the dispersive Boussinesq terms

$$\mathbf{V}_1 = \frac{{z_\alpha}^2}{2}\nabla(\nabla\cdot\mathbf{u}_{\alpha t}) + z_\alpha\nabla[\nabla\cdot(h\mathbf{u}_{\alpha t})] - \nabla\left[\frac{\eta^2}{2}\nabla\cdot\mathbf{u}_{\alpha t} + \eta\nabla\cdot(h\mathbf{u}_{\alpha t})\right] \tag{4}$$

$$\mathbf{V}_2 = \nabla\left\{(z_\alpha-\eta)(\mathbf{u}_\alpha\cdot\nabla)[\nabla\cdot(h\mathbf{u}_\alpha)] + \frac{1}{2}({z_\alpha}^2-\eta^2)(\mathbf{u}_\alpha\cdot\nabla)(\nabla\cdot\mathbf{u}_\alpha)\right\} + \frac{1}{2}\nabla\left\{[\nabla\cdot(h\mathbf{u}_\alpha) + \eta\nabla\cdot\mathbf{u}_\alpha]^2\right\} \tag{5}$$

The additional terms, $\mathbf{R}_b$, $\mathbf{R}_s$, and $\mathbf{R}_f$, represent the effects of wave breaking, subgrid lateral turbulent mixing, and bottom friction, respectively, as detailed in sections 2.3 and 2.4.

The fully nonlinear Boussinesq equations have improved dispersion characteristics in the case of large wave number and nonlinearity in shallow water. In connection with surface waves and wave-induced currents, it is worth mentioning that the equations are suitable for modeling wave-current interaction, as shown by *Kirby* [1997].

2.2. A Treatment of Moving Shorelines

To simulate swash motions, it is necessary for the model to include a treatment of the sea-land interface. Instead of tracking the wetted and dry cells during wave run-up/run-down on the beach, we treat the entire computational domain as an active fluid domain by employing an improved version of the slot or permeable-seabed technique proposed by *Tao* [1984] for the simulation of wave run-up. The original slot technique has been used by *Madsen et al.* [1997] in a Boussinesq model formulated in terms of mass flux and free surface elevation. The basic idea behind this technique is to replace the solid bottom, where there is very little or no water covering the land, by a porous seabed, or to assume that the solid bottom contains narrow slots. This allows the water level to be below the beach elevation. Figure 1 illustrates a beach with the presence of the slot.

The replacement of the solid bottom by narrow slots results in a modification of the mass equation shown by (1), where

$$\beta = \begin{cases} \delta + (1-\delta)e^{\lambda\frac{(\eta-z^*)}{h_0}}, & \eta \le z^* \\ 1, & \eta > z^* \end{cases} \tag{6}$$

and

$$\Lambda = \begin{cases} \delta + \gamma\left(e^{\lambda\frac{(\eta-z^*)}{h_0}} - e^{-\lambda\frac{(h_0+z^*)}{h_0}}\right), & \eta \le z^* \\ \frac{\eta-z^*}{\eta+h_0} + \frac{\delta(z^*+h_0)}{\eta+h_0} + \gamma\left(1 - e^{-\lambda\frac{(h_0+z^*)}{h_0}}\right), & \eta > z^* \end{cases} \tag{7}$$

Here $\gamma = \frac{(1-\delta)h_0}{\lambda(\eta+h_0)}$, δ is the relative width of slot with respect to a unit width of beach, λ is the parameter for the smooth transition from unity to δ, and h_0 is the offshore still water depth where a slot begins.

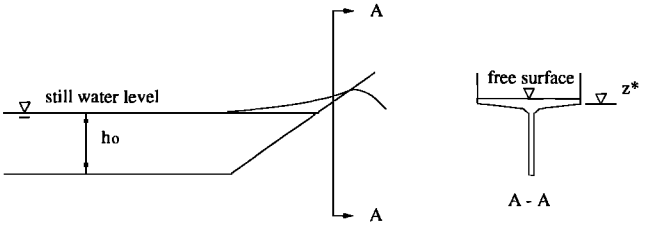

Figure 1. Schematic of a beach with the presence of a narrow slot.

Madsen et al. [1997] showed that, even though a very narrow slot width is used, there is still about a 10% error in the computed maximum run-up in comparison with the analytical solution by *Carrier and Greenspan* [1958]. This is attributed to the additional cross-sectional area introduced by the narrow slot, because the maximum run-up is very sensitive to the total volume of mass at the run-up tip. In contrast to *Tao*'s [1984] formulation, which does not conserve mass in the presence of a slot, we retain an equivalent cross-sectional area of a unit width of beach, leading to the improvement in the simulation of run-up as shown by *Kennedy et al.* [1999]. The modified seabed elevation z^* may be expressed as

$$z^* = \frac{z^s}{1-\delta} + h_0\left(\frac{\delta}{1-\delta} + \frac{1}{\lambda}\right) \tag{8}$$

in which z^s is the elevation of the solid seabed.

The optimal values of δ and λ are found to be 0.002 and 80, respectively, which give the best agreement with the analytical solution by *Carrier and Greenspan* [1958]. For simulations of wave run-up on steep slopes, however, a larger slot width and a localized filter may be needed to avoid numerical instability. *Chen et al.* [1999] verified the Boussinesq model with the improved permeable-seabed technique against the laboratory experiment on solitary wave run-up on a circular island described by *Liu et al.* [1995]. Good agreement between the computed and measured maximum run-up was found.

2.3. A Treatment of Wave Breaking

Attempts have been made in the literature to introduce treatments of wave breaking into Boussinesq models. They may be grouped into eddy viscosity [e.g., *Zelt*, 1991; *Karambas and Koutitas*, 1992; *Kennedy et al.*, 1999] and "roller" breaking models [e.g., *Schäffer et al.*, 1993; *Svendsen et al.*, 1996]. With respect to energy dissipation due to wave breaking, these two types of models give similar results as demonstrated by *Svendsen et al.* [1996]. For simplicity, we choose an eddy viscosity type model. Following *Kennedy et al.* [1999], the energy dissipation due to wave breaking in shallow water is modeled by introducing the momentum mixing terms:

$$R_b^x = \frac{1}{h+\eta}\left(\{\nu\left[(h+\eta)u_\alpha\right]_x\}_x + \frac{1}{2}\left\{\nu\left[(h+\eta)u_\alpha\right]_y + \nu\left[(h+\eta)v_\alpha\right]_x\right\}_y\right) \tag{9}$$

$$R_b^y = \frac{1}{h+\eta}\left(\frac{1}{2}\left\{\nu\left[(h+\eta)v_\alpha\right]_x + \nu\left[(h+\eta)u_\alpha\right]_y\right\}_x + \left\{\nu\left[(h+\eta)v_\alpha\right]_y\right\}_y\right) \tag{10}$$

where superscripts x and y represent the directions in the horizontal plane, subscripts x and y denote spatial differentials, and ν is the eddy viscosity localized on the front face of the breaking wave. It should be emphasized that the localization of the eddy viscosity is of importance for modeling nonlinear waves. In contrast, a global eddy viscosity would smear the asymmetry and skewness of the breaking waves in a nonphysical manner.

We define eddy viscosity as

$$\nu = B\delta^2|(h+\eta)\nabla\cdot\mathbf{M}| \tag{11}$$

in which δ is a mixing length coefficient with an empirical value of $\delta = 1.2 \sim 1.8$. The quantity B that controls the occurrence of energy dissipation with a smooth transition from 0 to 1 is given by

$$B = \begin{cases} 1, & \eta_t \geq 2\eta_t^* \\ \frac{\eta_t}{\eta_t^*} - 1, & \eta_t^* < \eta_t \leq 2\eta_t^* \\ 0, & \eta_t \leq \eta_t^* \end{cases} \tag{12}$$

Figure 2 illustrates wave breaking on a barred beach and the momentum mixing associated with the roller. In analogy to the roller model by *Schäffer et al.* [1993], we determine the onset and cessation of wave breaking using the parameter η_t^*, which is defined as

$$\eta_t^* = \begin{cases} \eta_t^{(F)}, & t \geq T^* \\ \eta_t^{(I)} + \frac{t-t_0}{T^*}(\eta_t^{(F)} - \eta_t^{(I)}), & 0 \leq t - t_0 < T^* \end{cases} \tag{13}$$

where T^* is the transition time, t_0 is the time when wave breaking occurs, and $t - t_0$ is the age of the breaking event. The value of $\eta_t^{(I)}$ is chosen between $0.35\sqrt{gh}$ and $0.65\sqrt{gh}$, while the values of $\eta_t^{(F)}$ and T^* are $0.15\sqrt{gh}$ and $5\sqrt{h/g}$, respectively. The construction and verification of the breaking model are detailed by *Kennedy et al.* [1999]. The lower limit of the empirical coefficient $\eta_t^{(I)}$ is found to be more suitable to bar/trough beaches, while the upper limit gives optimal agreement for waves breaking on monotone sloping beaches. *Chen et al.* [1999] describe the implementation and verification of the breaking model in two horizontal dimensions.

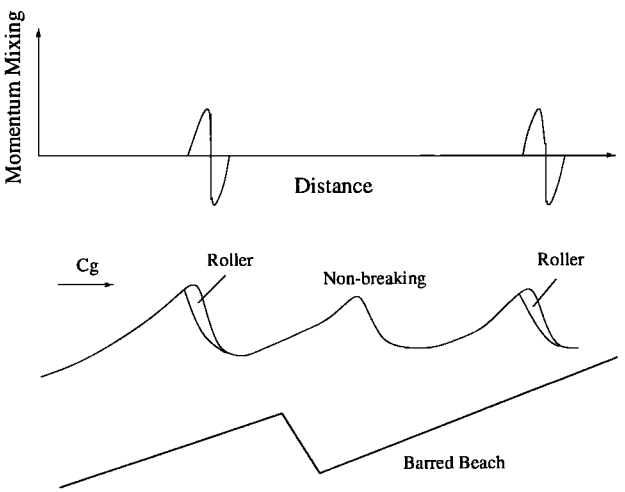

Figure 2. Schematic of wave breaking on a barred beach.

2.4. Subgrid Turbulent Mixing and Bottom Friction

Boussinesq models are based on vertically integrated mass and momentum equations. However, the grid size involved with the simulation of surface waves is usually smaller than the typical water depth. The horizontally distributed eddy viscosity resulting from subgrid turbulent processes may therefore become an important factor influencing the flow pattern of the wave-generated current field. In the absence of the subgrid model in the governing equations, the underlying current field generated by wave breaking may become so chaotic that no realistic flow pattern can be recognized. In the present study, we utilize the Smagorinsky-type subgrid model [Smagorinsky et al., 1965] to account for the effect of the resultant eddy viscosity on the underlying flow.

$$R_s^x = \frac{1}{h+\eta}\left(\{\nu_s\left[(h+\eta)u_\alpha\right]_x\}_x + \frac{1}{2}\left\{\nu_s\left[(h+\eta)u_\alpha\right]_y + \nu_s\left[(h+\eta)v_\alpha\right]_x\right\}_y\right) \quad (14)$$

$$R_s^y = \frac{1}{h+\eta}\left(\frac{1}{2}\left\{\nu_s\left[(h+\eta)v_\alpha\right]_x + \nu_s\left[(h+\eta)u_\alpha\right]_y\right\}_x + \left\{\nu_s\left[(h+\eta)v_\alpha\right]_y\right\}_y\right) \quad (15)$$

where ν_s is the eddy viscosity due to the subgrid turbulence.

$$\nu_s = c_m \Delta x \Delta y \left[(U_x)^2 + (V_y)^2 + \frac{1}{2}(U_y + V_x)^2\right]^{\frac{1}{2}} \quad (16)$$

in which U and V are the velocity components of the time-averaged underlying current field; Δx and Δy are the grid spacing in the x and y directions, respectively; and c_m is the mixing coefficient with a default value of 0.25. In the course of simulation, we obtain the underlying current field by averaging the instantaneous velocity over two wave periods and update ν_s accordingly.

As usual, the bottom friction is modeled by the quadratic law

$$\mathbf{R_f} = \frac{f}{h+\eta}\mathbf{u}_\alpha|\mathbf{u}_\alpha| \quad (17)$$

where the friction coefficient is chosen to be $f = 6.0 \times 10^{-3}$ in the present simulation. This value is about 2 orders of magnitude larger than the friction coefficient used by *Zelt* [1991] in his Boussinesq model for solitary wave run-up on a 1:20 sloping bottom, but it is about 1 order of magnitude smaller than the bottom friction coefficients used to compute longshore currents generated in laboratories (e.g., $k \approx 5.0 \times 10^{-2}$ of *Kobayashi et al.* [1997]). Notice that $\mathbf{u}_\alpha$ is the velocity vector for the combined wave and current motion. Under field conditions, owing to the variability of hydrodynamic and morphologic characteristics, spatially variable friction coefficients are likely to be used.

Following *Wei et al.* [1995], quasi fourth-order finite difference schemes are used to solve the governing equations described above. The numerical model has been extensively tested against laboratory measurements by *Wei et al.* [1995], *Wei* [1997], *Kennedy et al.* [1999], and *Chen et al.* [1999]. We shall use this model to study wave-induced nearshore circulation and vortex structures associated with rip currents.

3. Simulation of Rip Currents

3.1. Topography and Model Setup

A beach with offshore sand bars incised by rip channels is a common type of bathymetry in many coastal regions. Figure 3 shows the bathymetry and the contours of the water depth used for the simulation of rip currents in the present study, which was inspired by a physical experiment conducted at the University of Delaware [see *Haller et al.*, 1997]. To save computational efforts, only half of the experimental topography is used in the numerical simulation, assuming symmetry about the cross-shore center line of the physical wave basin. We construct the topography on the basis of the bathymetric data from the laboratory experiment. The numerical wave basin is 19 m long and 9.1 m wide. As depicted in Figure 3a, a 1.8 m wide rip channel interrupts a submerged bar on a beach with a 1:30 slope. The water depth of the offshore flat bottom is 0.373 m. The averaged water depths on the crest and at the offshore toe of the bar are 0.048 and 0.1 m, respectively. Each of the bar sections spans 1.25 m in the cross-shore direction and 3.65 m in the longshore direction. As shown in Figure 3b, the bathymetry is slightly asymmetric.

We use a normally incident, monochromatic wave train with a period of 1.0 s and wave height of 4.8 cm as input to the model. Waves are generated by the source function technique as detailed by *Wei et al.* [1999]. The wave generation is located internally at $x = 4.0$ m, and a damping sponge layer is put behind the source line to absorb outgoing waves reflected by the submerged bar and the sloping beach. The grid size is 0.05 and 0.1 m in the cross-shore and longshore directions, respectively. The time step is chosen to be 0.02 s.

3.2. Model Results

The Boussinesq model provides a time series of free surface elevation and velocity components for the combined wave and current motion. These results are used to obtain many useful quantities, including radiation stress, mean water level, wave height, underlying current field, and vorticity field associated with the wave-induced nearshore circulation.

Figure 4 illustrates the computed mean water level averaged over two wave periods, and the locations of wave breaking after 20 s have elapsed in the simulation. Obviously, wave breaking causes a cross-shore variation

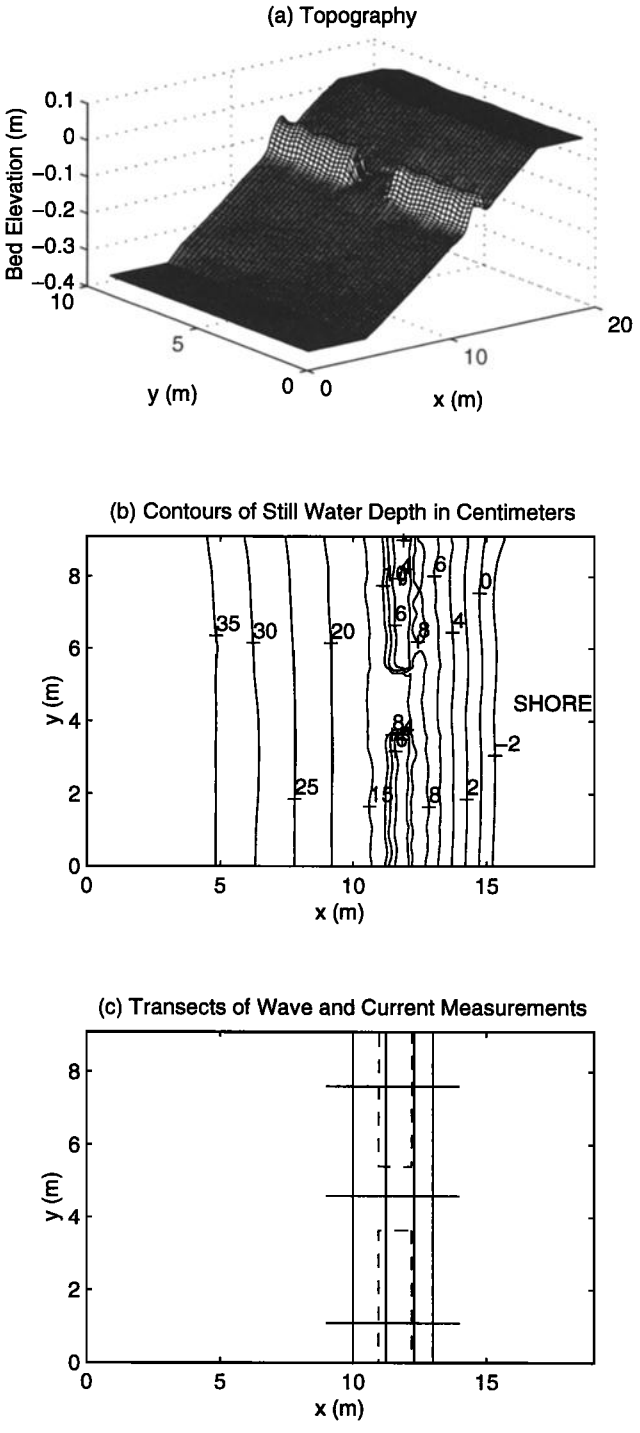

Figure 3. Topography of a barred beach with a rip channel and the locations of measurements: (a) topography, (b) contours of still water depth, and (c) transects of wave and current measurements. The dashed lines in Figure 3c denote the bar footprint.

of radiation stresses that creates the setup of the mean free surface. On the other hand, longshore variations of radiation stresses also exist owing to the presence of the rip channel. The shaded areas in Figure 4c display the computed locations of wave breaking over two wave periods. We notice that waves break on the submerged bar and near the shoreline on the barred beaches, while at the rip channel, wave breaking mainly occurs near the shoreline. The difference in the breaking locations results in the longshore gradient of the mean free surface. The resultant pressure gradient is believed to be one of the driving forces for rip currents on barred beaches as suggested by *Dalrymple* [1978].

In Figure 4b, the dashed lines denote the footprint of the submerged bar. From the contour map of the

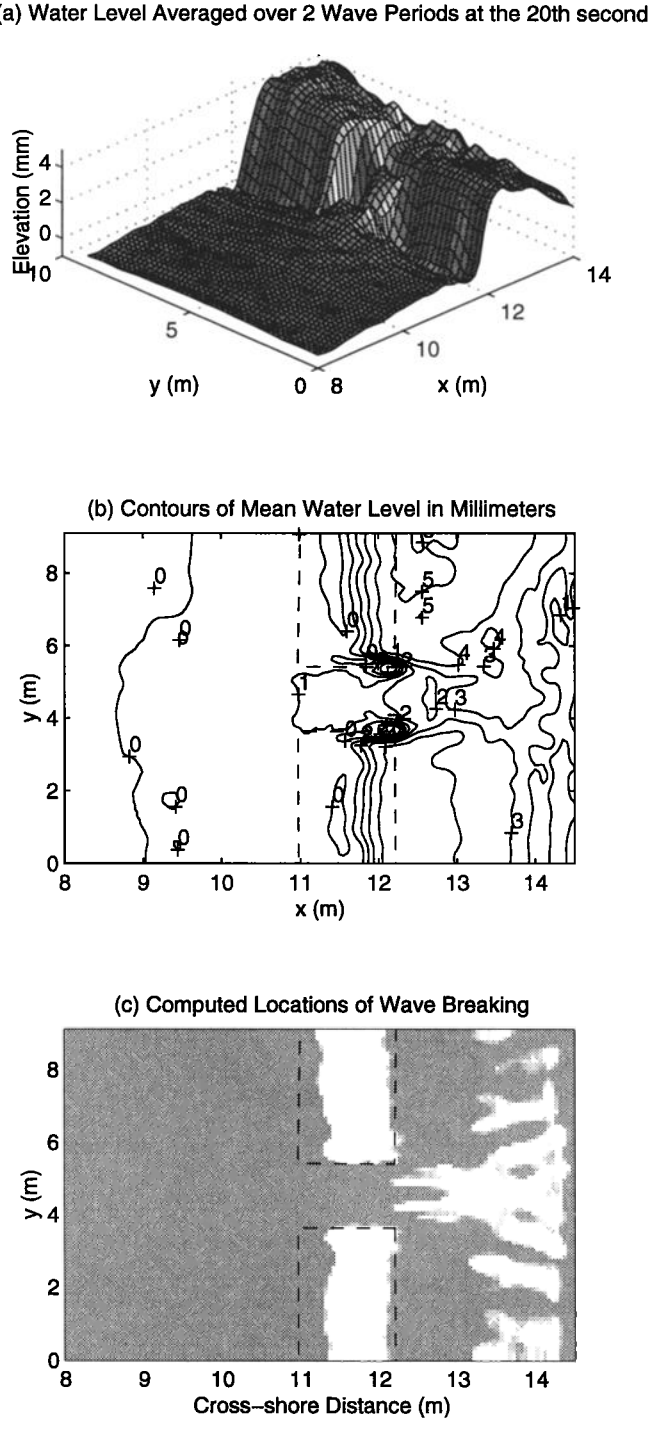

Figure 4. Modeled mean free surface and the locations of wave breaking (denoted by shading) averaged over two wave periods ($t = 18 \sim 20$ s): (a) mean water level, (b) contours of water level, and (c) locations.

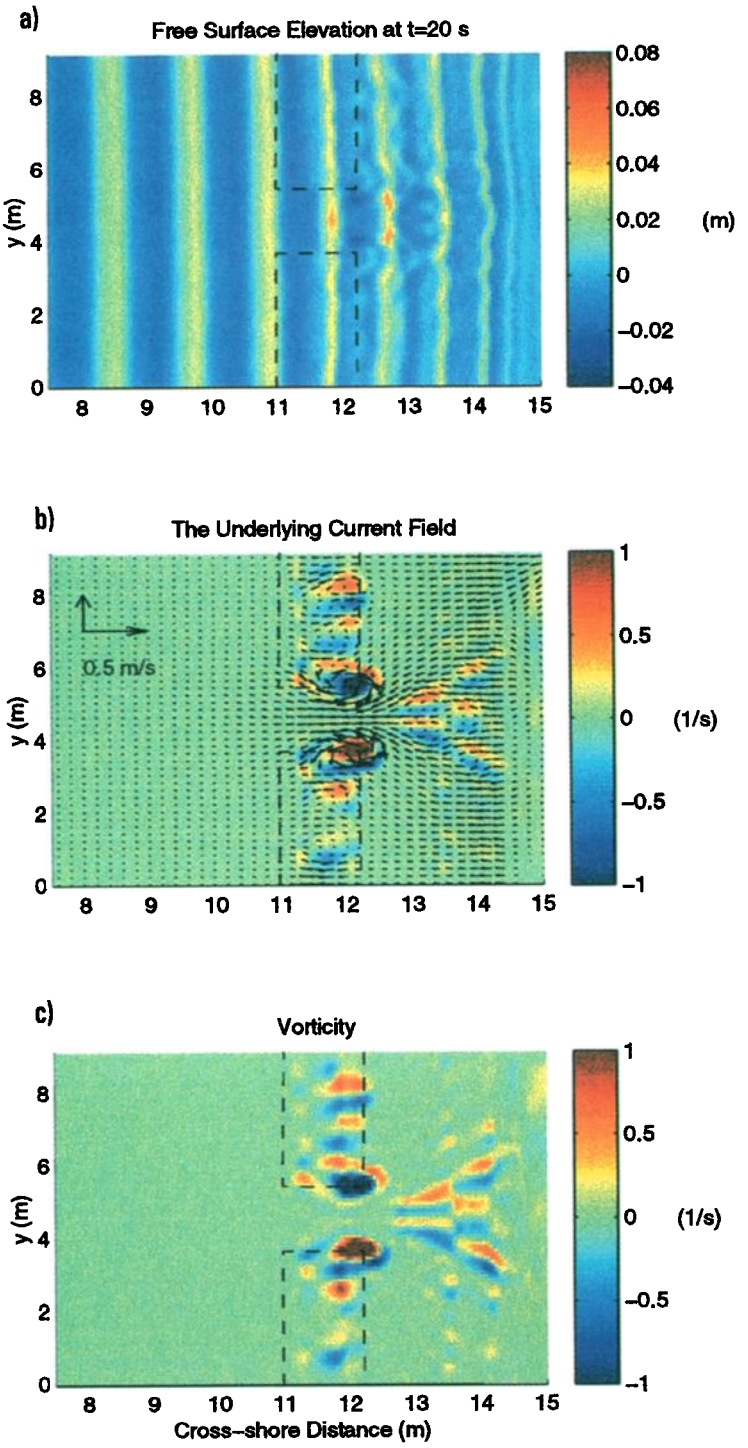

Plate 1. A snapshot of (a) the computed free surface elevation, (b) the underlying current field and associated mean vorticity, and (c) the instantaneous vorticity field at $t = 20$ s.

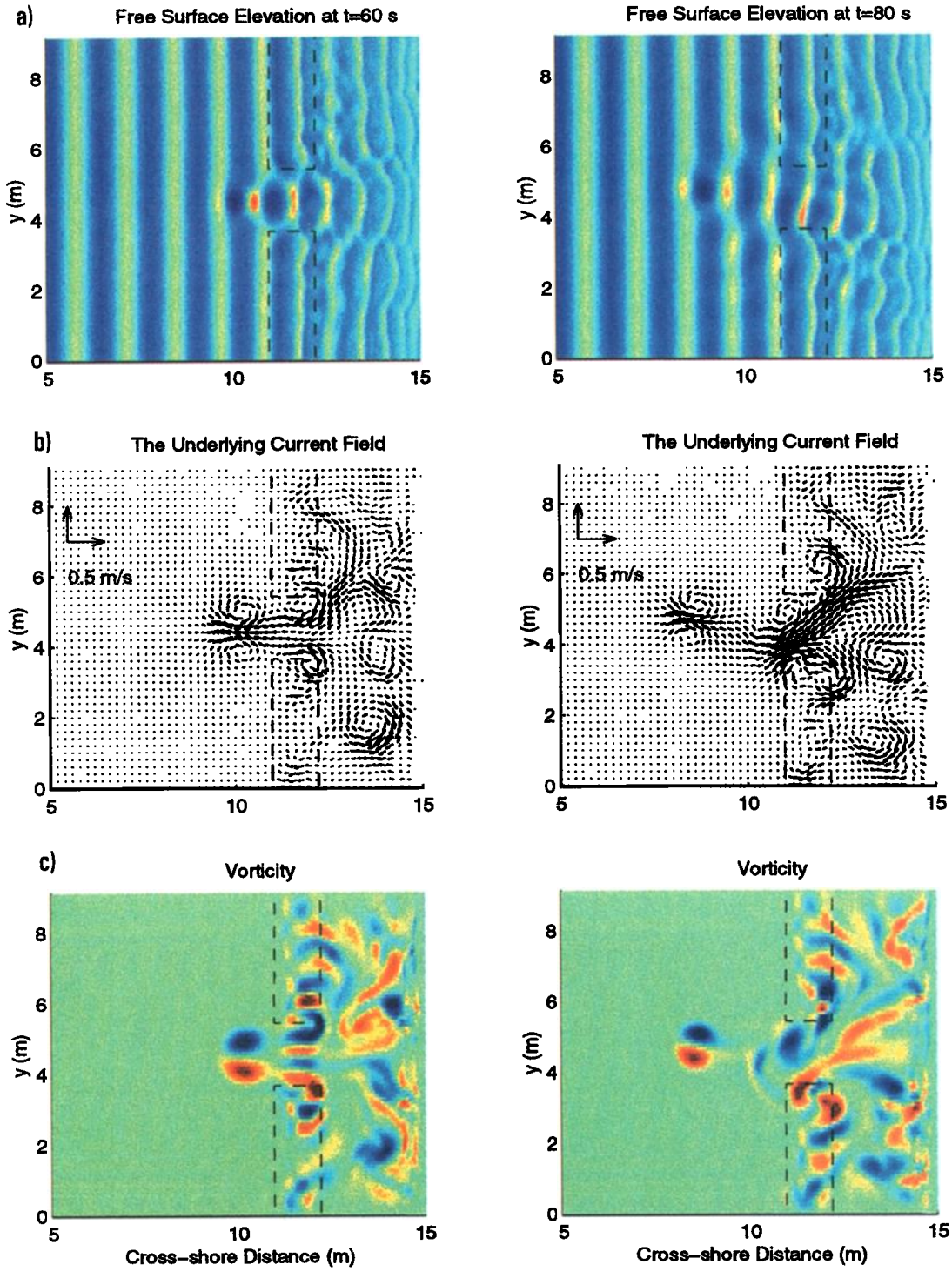

Plate 2. Snapshots of (a) the computed free surface elevation, (b) the underlying current field, and (c) vorticity at (left) $t = 60$ s and (right) $t = 80$ s.

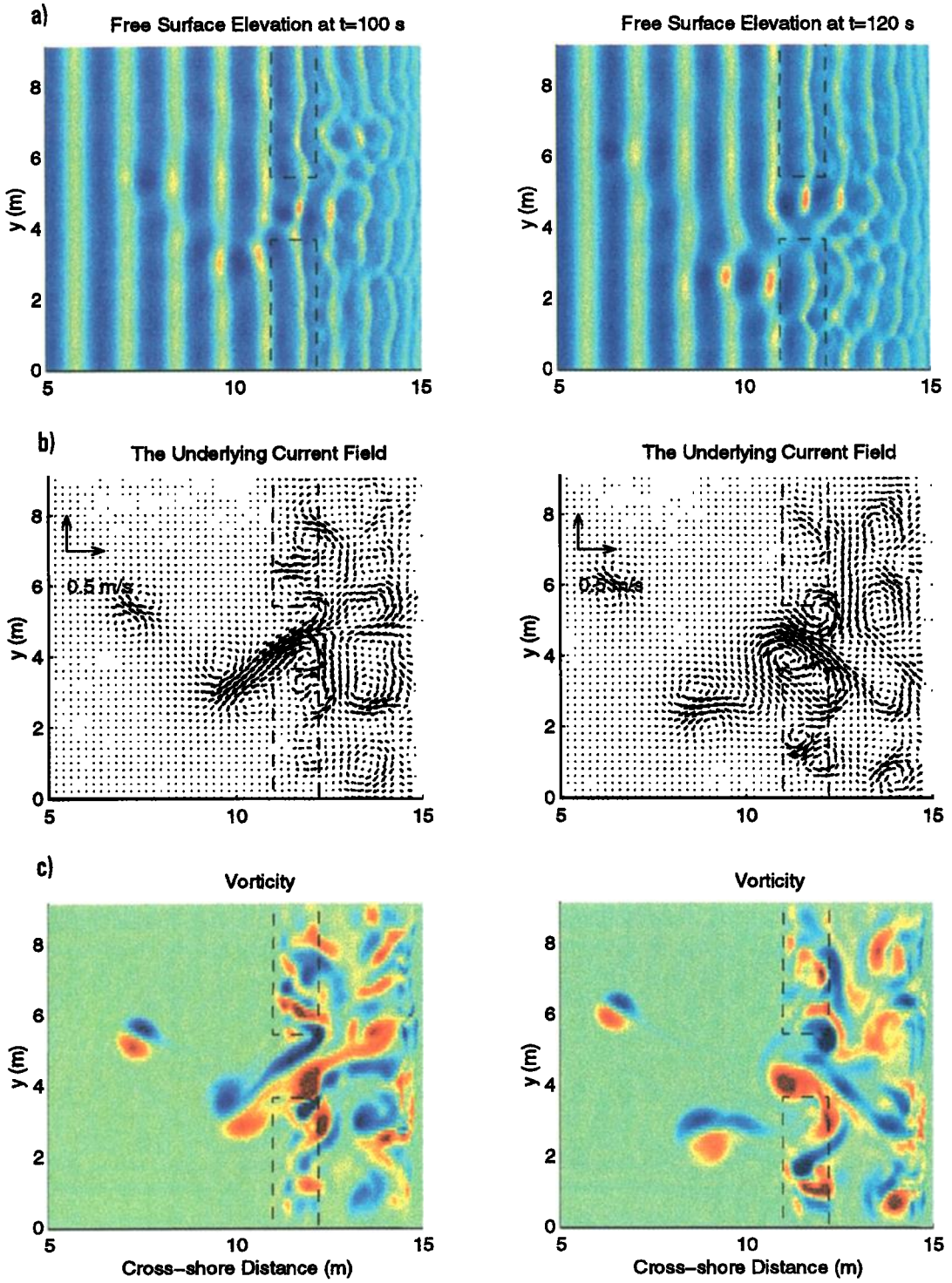

Plate 3. Snapshots of (a) the computed free surface elevation, (b) the underlying current field, and (c) vorticity at (left) $t = 100$ s and (right) $t = 120$ s.

mean free surface, it is noticeable that two depressions of mean water level appear on the edges of the rip channel. They are located at the eyes of the vortex pairs as shown in Plate 1. The mean water levels on both sides of the rip channel are not equal because of the slight asymmetry in the bathymetry.

Plate 1 presents a snapshot of the computed free surface elevation, the underlying current field, and the vorticity developing on the bar crest and near the shoreline at the 20th s of simulation. The vorticity is defined as $\Omega_\alpha = v_x - u_y$, where (u,v) can be either the instantaneous velocity components (u_α,v_α) or the underlying current (U, V) averaged over two short wave periods. The waves propagate from left to right. In Plate 1a, blue denotes the wave trough and yellow and red are the wave crest. The unit of the color bar for the free surface elevation is in meters, while that for vorticity is s^{-1}. The dashed lines once again represent the bar footprint. Owing to the effects of nonlinear shoaling, the wave crest becomes peaky on the bar crest. It is noticeable that the wave height in the rip channel is higher than the wave height on the bar crest because of wave-current interaction and the absence of wave breaking in the channel.

We obtain the underlying current field driven by the breaking waves by averaging the modeled fluid particle velocity over two wave periods. The velocity, as one of the dependent variables of the extended Boussinesq equations, is located at the elevation of z_α = -0.531h in the water column. Assuming a fairly depth uniform underlying flow, the computed velocity of the current field can be taken as the depth-averaged velocity of the flow.

In Plate 1b, we notice that a pair of vortices develops on the edges of the rip channel. As mentioned above, the eddies cause the depression of the mean water level with the magnitude of about half the maximum setup of mean free surface in the present case. The mechanism of the vortex production is attributed to the strong velocity shear associated with the rip current in the area between the channel and the submerged bar. We compute the onshore mass flux due to the wave motion based on the modeled results and find that the onshore mass flux of wave motion over the submerged bar is much greater than that in the rip channel as expected. This longshore gradient of mass flux also contributes to the vortex generation. A comparison of Plates 1b and c shows that the vorticity in Plate 1b computed from the underlying current field is in agreement with that directly calculated from the instantaneous velocity of the combined wave and current motion as depicted by Plate 1c. The absence of spatial periodic features at the scale of the wave length in the instantaneous vorticity plots implies that there is a separation between the underlying rotational flow and the wave motion. In addition to the vortex pair on the edges of the rip channel, vortices also appear on the bar crest and near the shoreline behind the rip channel. The vorticity on the crest of the bar originates from the longshore nonuniformity of breaking on the bar crest because of the perturbations in the bathymetry. This is similar to the mechanism of vortex generation due to nonuniformities in bores as suggested by *Peregrine* [1998].

The vortex generation and vorticity transport may be explained by the vorticity equations derived from the momentum equations (3). Taking the curl of (3) leads to

$$\Omega_{\alpha t} + (\mathbf{u}_\alpha \cdot \nabla)\,\Omega_\alpha = -\Omega_\alpha \nabla \cdot \mathbf{u}_\alpha + \nabla \times \mathbf{R}_b + \nabla \times \mathbf{R}_s - \nabla \times \mathbf{R}_f + O(\mu^2 \frac{gh}{L^2}) \quad (18)$$

in which Ω_α is the vertical component of the vorticity vector at the reference elevation z_α and $\Omega_\alpha = \nabla \times \mathbf{u}_\alpha$. Notice that μ is the measure of wave dispersion and $\mu \ll 1$ in the surf zone, where the water depth h is much smaller than the wave length L. Clearly, $\nabla \times \mathbf{R}_b$ is the source of vorticity caused by the longshore variation of wave breaking. The bottom friction and subgrid mixing serve as the dissipation agent of vorticity. Owing to the nonzero depth variation of vertical velocity, the first term on the right-hand side of the vorticity equation provides the mechanism of vortex stretching.

To illustrate the spatial and temporal variability of the the rip current and nearshore circulation, we present a time sequence of the computed wave field, underlying current field, and vorticity in Plate 2 and Plate 3. The time interval between each snapshot of the model results is 20 s. As depicted by the sequence of computed flow field, the modeled rip current meandered at the rip channel exit. *Haller et al.* [1997] observed that the longshore component of the current measured at the rip channel exit oscillated with an averaged period of 17~20 s in the physical experiment. Owing to the computational limits, however, the numerical model did not run long enough to allow for a spectral analysis of the rip oscillation.

Several interesting phenomena are observed from the time sequence of the model results. First, the wave field behind the submerged bar is no longer long crested. The development of the rip current and circulation cells causes the wave crest to be refracted as illustrated by the computed free surface imagery. Because of the release of higher harmonics after the wave passage over the submerged bar, secondary crests are found in the surf zone when we examine the cross-shore free surface profiles on the barred beaches. Second, vortices continue to grow on the bar crest and near the shoreline and they merge as shown in Plate 2c, left. From Plate 2c, right, we notice that the first pair of vortices is shed offshore, followed by a second pair. The rip current is accompanied by strong vortices. Third, the computed flow fields averaged over two wave periods show that the rip current is unstable and oscillates in the rip channel. As time goes on, the vorticity field in the surf zone becomes very complex and vortices seaward of the channel exit appear to move alongshore rather than being

directly transported offshore (Plate 3c, right). This becomes more clear at the later stage of simulation and is confirmed by the mean current field averaged over a long period of time as shown in the next subsection.

The rip instability results in the oscillation of rip current and prevents the vortices from being convected far offshore. The vanishing of rip currents away from the exit of the rip channel could be of significance, in practice. It implies that sediments or pollutants might not be transported offshore by the rip current itself. Instead, they may stay in the area seaward of the submerged bar or be transported away by other mechanisms. As observed in the laboratory experiment, floaters deployed in the surf zone flowed out through the rip channel but most of them did not move far away offshore. They returned to the surf zone over the submerged bar by the surface drift of the waves and probably by eddies associated with the rip current.

3.3. Model/Data Comparison

The laboratory experiment on rip current generation with a similar topography by *Haller et al.* [1997] provides an ideal test case for model verification. The physical wave basin is twice the size of the numerical wave basin and has two rip channels. A detailed description of the laboratory experiment is given by *Haller et al.* [1997]. In the following, we shall compare time-averaged properties of the combined wave and current motion predicted by the numerical model and measured from the physical experiment. It is worth mentioning that the laboratory data were averaged over the last half of the data collection period (819 s) to eliminate the effects of transients in the wave basin. Owing to the computational limit, the numerical results are averaged over 180 wave periods after the first wave arrives at the shoreline. This averaging time is about 1 order of magnitude shorter than it is in the physical experiment.

Figure 5 and Figure 6 present the comparison of the computed and measured wave height and mean water level along three cross-shore transects. Two transects (y = 1.1 and 7.6 m) are located on the barred beach near the sidewalls of the numerical wave basin, while the other (y = 4.6 m) is along the center line of the rip channel in the cross-shore direction. The circles represent the laboratory data, while the numerical results are denoted by stars. We compute the root-mean-square wave height (H_{rms}) and the mean water level by averaging the numerical results over 180 wave periods.

Despite a slight discrepancy along the transect of y = 1.1 m, which might result from the use of only half the experimental wave basin by the numerical model, the agreement between the computed results and measurements along the cross-shore transects of the barred beach and the rip channel is satisfactory. We also notice that the wave heights at the offshore toe of the submerged bar are somewhat overestimated. Nevertheless, the Boussinesq model predicts reasonably well the decay of wave height due to wave breaking and the resultant setup of the mean water level in comparison with the laboratory measurements.

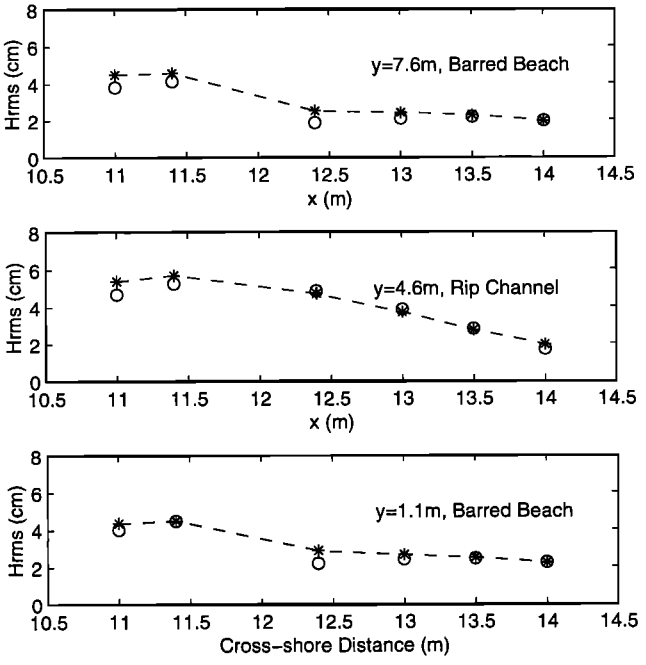

Figure 5. Comparison of computed (stars) and measured (± 0.2 cm) (circles) wave height.

Next, we compare the computed mean current with measurements as shown in Figure 7 and Figure 8. The velocity components are considered along four longshore transects. The transect of x = 10 m is seaward of the channel exit, and x = 13 m is shoreward of the submerged bar. The other two transects (x = 11.25 and 12.3 m) cross the rip channel. We obtain the modeled current speed by averaging the computed instantaneous fluid particle velocities over 180 s.

Figures 7 and 8 show that the modeled velocity components agree reasonably well with the measurements. First, the Boussinesq model captures well the spatial variation of the time-averaged, measured rip current. For instance, the model predicts the same signature of vanishing rip current seaward of the channel exit (i.e., transect x = 10 m) and the convergence of the rip current near the channel entrance (i.e., transect x = 12.3 m). Second, the maximum cross-shore and longshore currents are also predicted correctly by the numerical model as illustrated by the good agreement along the x = 12.3 and 13.0 m transects, respectively. The Froude number at the rip neck is about 0.2, which causes significant effects to the surface waves.

A comparison of the computed and measured mean current field is presented in Figure 9. The flow pattern predicted by the numerical model is similar to the measured velocity field. The rip instability diminishes the mean current in front of the channel exit because of the meandering of the rip current. As the topography is not perfectly symmetric about the center line of

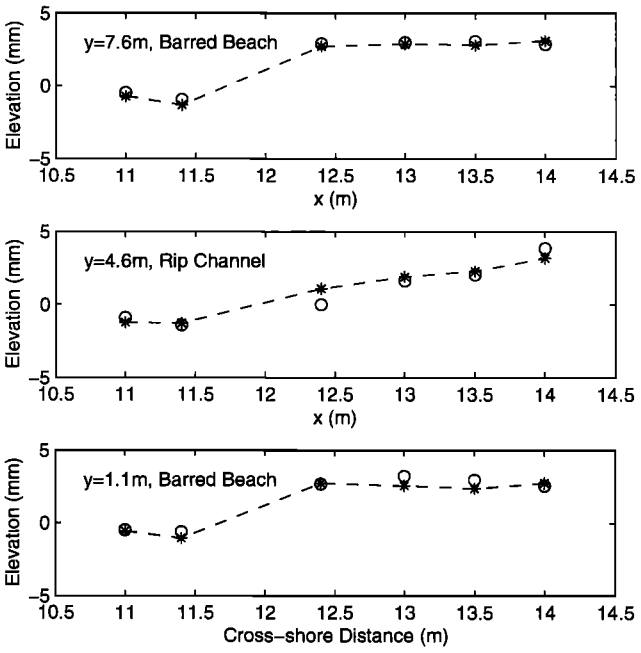

Figure 6. Comparison of computed (stars) and measured (circles) mean water level.

the rip channel, the mean rip current averaged over a long period of time has a slight bias toward one side of the channel. There is a shoreward mean flow and secondary circulation close to the shoreline. This can be attributed to the larger wave setup at the shoreline shoreward of the rip channel in comparison with that shoreward of the submerged bar.

Notice that the averaging time (180 s) for the numerical data covers about a period of the very low frequency motion (> 100 s) and about 10 periods of the rip oscillation (17 ~ 20 s) observed in the laboratory experiment of *Haller et al.* [1997]. Both numerical results and laboratory measurements suggest a large degree of temporal and spatial variability in the rip current system. As an attempt to measure the degree of variability, we compute the standard deviation of the time series of mean surface elevation and cross-shore and longshore currents. The time series is obtained by time averaging the instantaneous surface elevation and particle velocity every two wave periods from both numerical results and laboratory measurements.

Figure 10 depicts the root-mean-square (RMS) values of the computed and measured mean water levels along three cross-shore transects, i.e., y = 7.6, 4.6, and 1.1 m. The RMS values of the temporal variation of wave setup agree reasonably well with the measured data. Figure 11 and Figure 12 show the comparison of the RMS values of the computed and measured cross-shore and longshore currents along four longshore transects. Although the numerical results appear to overpredict the degree of temporal variability in the short-wave-averaged currents near the rip channel exit, the overall agreement is satisfactory.

4. Effects of Bathymetric Uniformity on Rip Stability

4.1. An Ideal Topography

In agreement with observations in the physical experiment, the numerical results as shown in the preceding section indicate that the rip current is unstable. One may ask whether the rip current is stable if there are no perturbations in the bathymetry and in the mean free surface. This section is therefore devoted to answering this question.

We construct an ideal topography by averaging the cross-shore profiles of the barred beach from the bathymetric data taken during the laboratory experiment. This process filters out the perturbations and leads to a longshore uniform barred beach with a rip channel in the middle of the bar as shown in Figure 13. The basic configuration of the bathymetry and the numerical model setup are identical to those described in the previous section.

4.2. Delayed Rip Instability

The rip current generation and associated nearshore circulation are simulated using the ideal bathymetry. Interesting phenomena are observed from the numerical

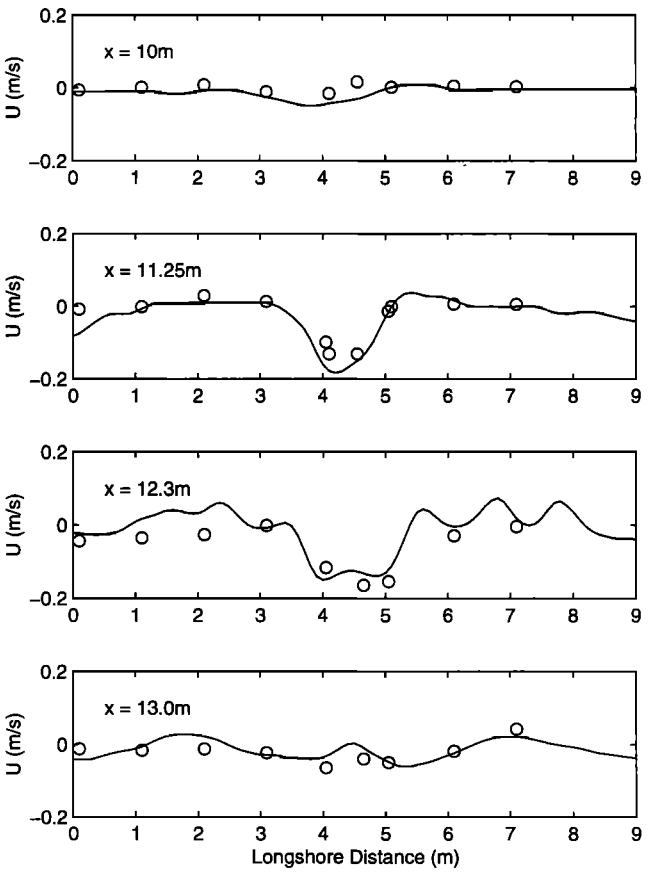

Figure 7. Comparison of computed (solid lines) and measured (± 0.005 m/s) (circles) cross-shore mean velocity.

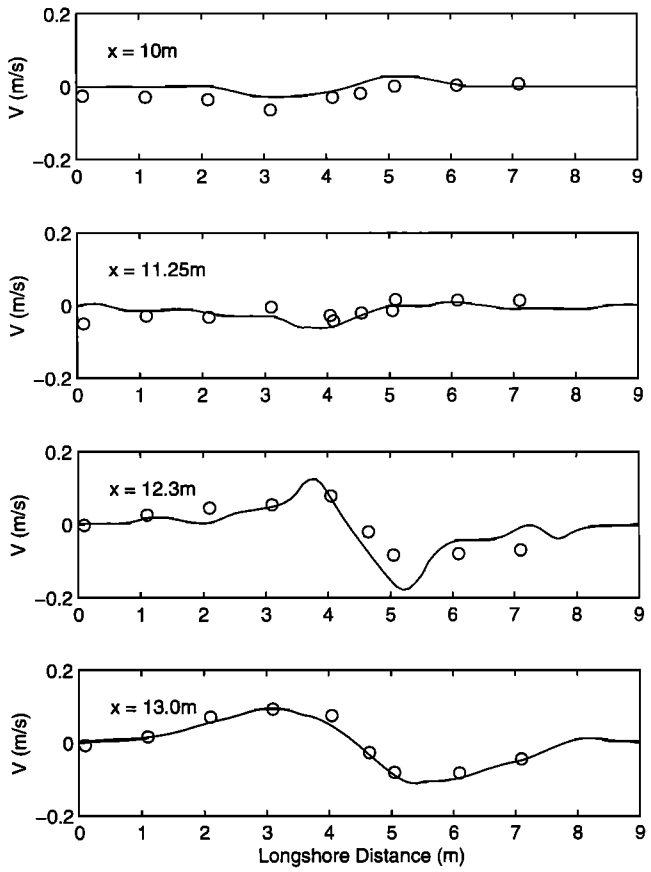

Figure 8. Comparison of computed (solid lines) and measured (± 0.005 m/s) (circles) longshore mean velocity.

experiment. It turns out that the spatial and temporal variation of the rip current and the vortex structure are significantly different from those utilizing the experimental bathymetry. Plate 4 and Plate 5 present the wave fields, the underlying current fields, and the associated vorticity fields at four different instants based on the numerical results.

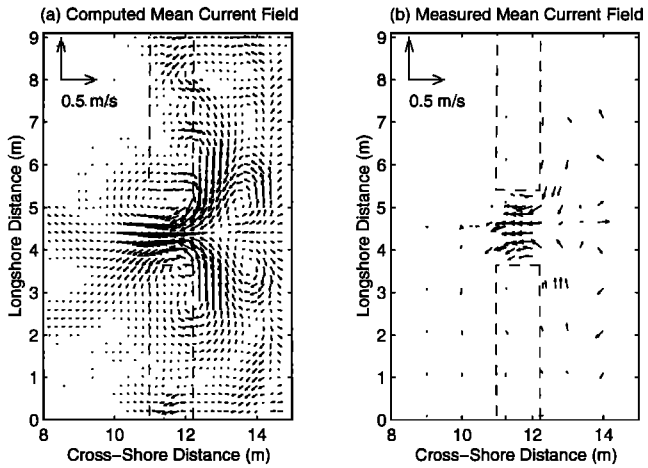

Figure 9. Comparison of the (a) computed and (b) measured mean current fields.

At the early stage of simulation, for instance, at the 20th s as shown in Plate 4c, left, a pair of vortices similar to the case with the experimental topography is developing on the edges of the rip channel (see Plate 1c). However, no vortices appear on the bar crest owing to the absence of bathymetric perturbation on the crest of the submerged bar in the ideal topography. We notice the first pair of vortices is shed offshore, followed by other pairs. In contrast to the case with the experimental bathymetry, the rip current remains stable in the first 120 s of simulation. The rip current flows straight offshore as depicted by Plate 5c, left. An interesting phenomenon of wave diffraction by the rip current is also observed in the same figure, which shall be discussed in detail in the next section.

After about 2 min of simulation, the instability starts developing and the rip current becomes unstable as illustrated in Plate 5c, right. The rip current cannot maintain a flow straight offshore. It meanders and oscillates back and forth in the rip channel as the simulation time goes on. Circulation cells behind the submerged bar are no longer symmetric. In the present simulation, although there are no bathymetric perturbations, there is actually a perturbation in the geometry of the numerical wave basin because the model topography is not perfectly symmetric about the center line of the rip channel when $\Delta y = 0.1$ m is used. The lack of bathymetric perturbations delays the rip instability, but the slight geometric asymmetry eventually leads to an unstable rip current as demonstrated in Plate 5. Our numerical experiment with a perfectly symmetric ideal bathymetry confirms the effect of the geometric pertur-

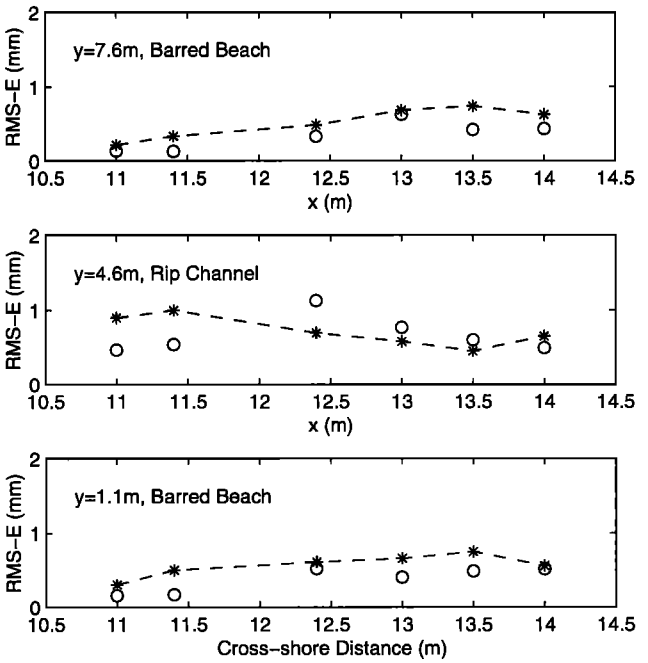

Figure 10. Comparison of the root-mean-square values of computed (stars) and measured (circles) mean water level.

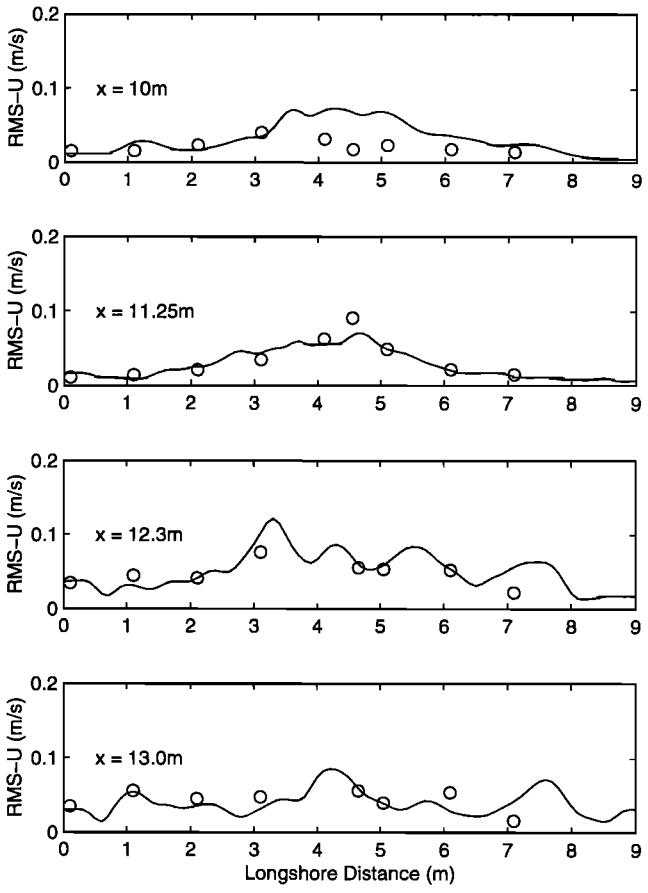

Figure 11. Comparison of the root-mean-square values of computed (solid lines) and measured (circles) cross-shore current.

bation and suggests that the accumulation of computer round-off errors may also provide the seed for the rip instability if the simulation is sufficiently long.

4.3. Similar Mean Quantities

For the ideal bathymetry, Figure 14 and Figure 15 give comparisons of the root-mean-square wave heights and mean water levels along three cross-shore transects identical to those in the case of experimental bathymetry. The computed H_{rms} and mean water level are again averaged over 180 s. First, we notice that the computed wave height near the channel exit is much greater than the measurements. This is attributed to the effects of the strong rip current on the wave transformation seaward of the rip channel. As shown in the next figures, the strength of the rip current near the channel exit is overpredicted owing to the delayed rip instability. Despite the overestimates of wave height in the rip channel, the agreement between the computed results and measurements along the transects crossing the submerged bars is fairly good. The difference in wave height in the rip channel does not appear to substantially affect the agreement of the mean water level along the center line of the channel in the cross-shore direction, although it slightly increases the setup inside the rip channel. The fairly good agreement between the computed and measured mean water levels suggests that the lack of bathymetric perturbations does not markedly change the long-term-averaged forcing of pressure gradient for the rip current generation.

Comparisons of the computed and measured mean velocity components along four longshore transects are given in Figure 16 and Figure 17. The four transects are located in the rip channel area, which are identical to those in the case of experimental bathymetry. The modeled mean velocity components are obtained by averaging the numerical results over 180 s. Fair agreement between the computed mean currents and measurements is observed. In comparison with the model results of experimental topography, the ideal bathymetry generates a broader but weaker rip current at the channel entrance as shown by the cross-shore velocity profile at x = 12.3 m. Because the same average time in the case of experimental bathymetry is used to compute the mean current, the delayed rip instability owing to the lack of bathymetric perturbation leads to an overprediction of the rip strength in front of the channel. As the rip current is also unstable in the case of ideal bathymetry, we expect that the persistence of the rip current near

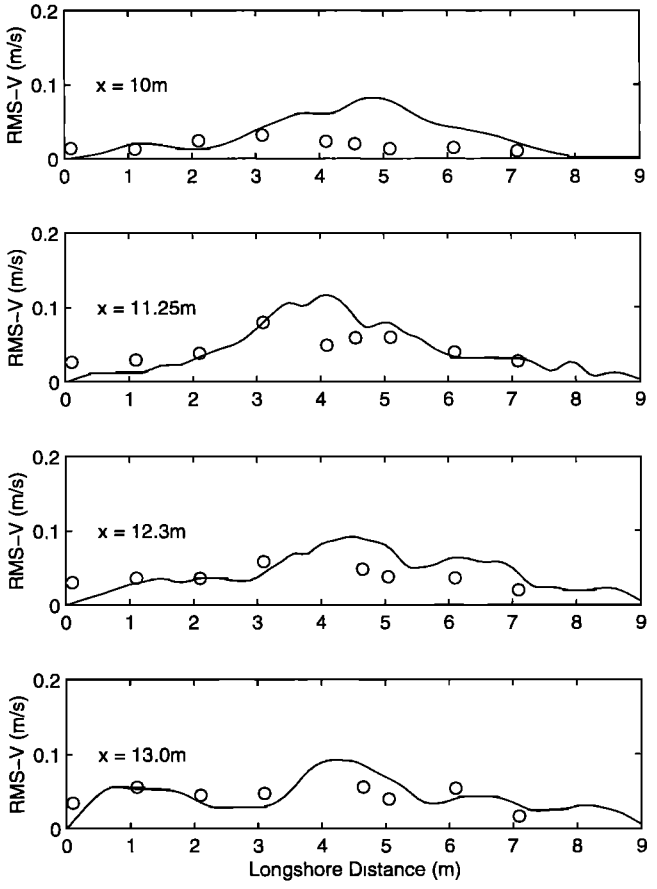

Figure 12. Comparison of the root-mean-square values of computed (solid lines) and measured (circles) longshore current.

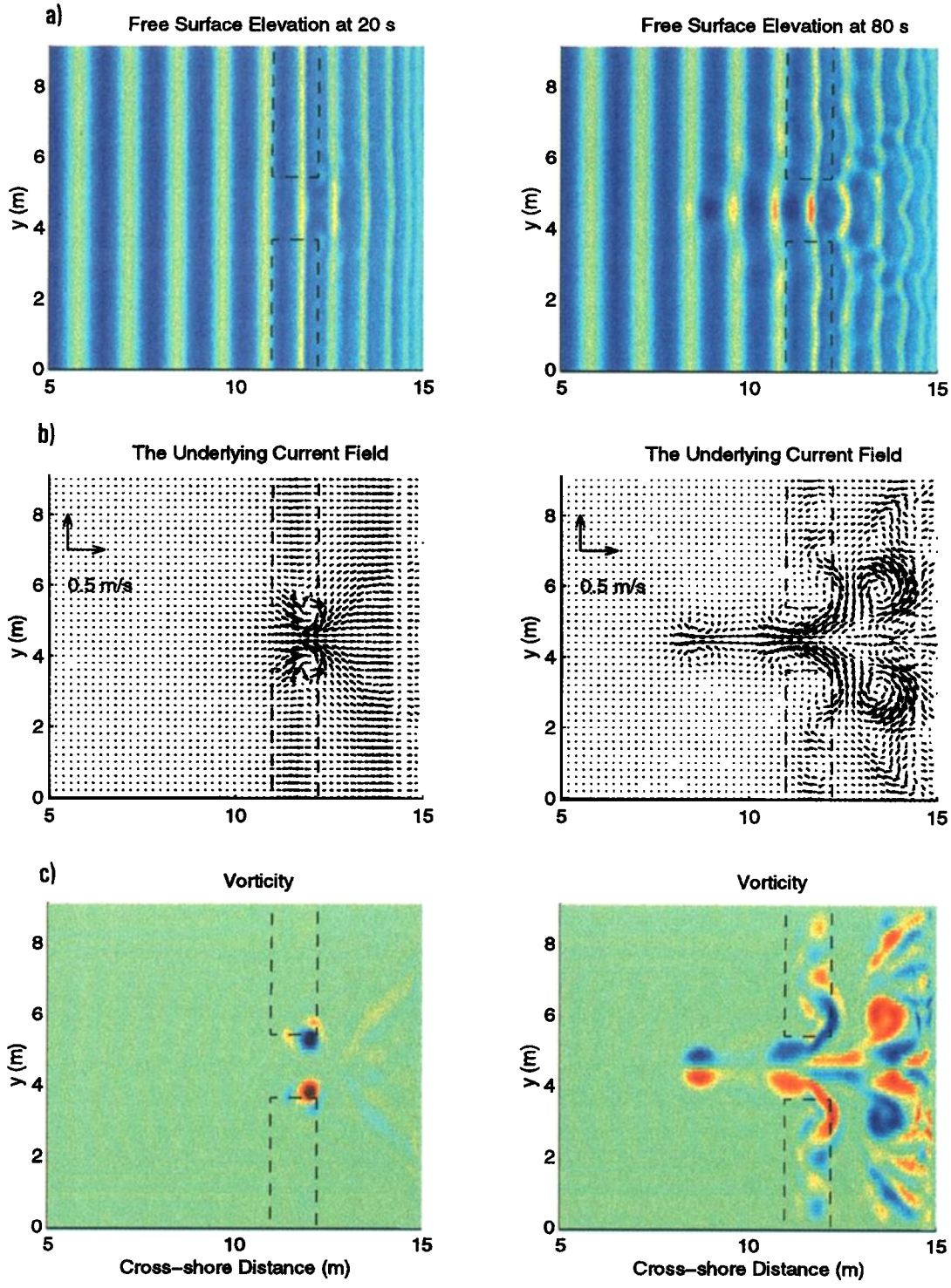

Plate 4. Computed (a) wave field, (b) underlying current, and (c) vorticity field at (left) $t = 20$ s and (right) $t = 80$ s.

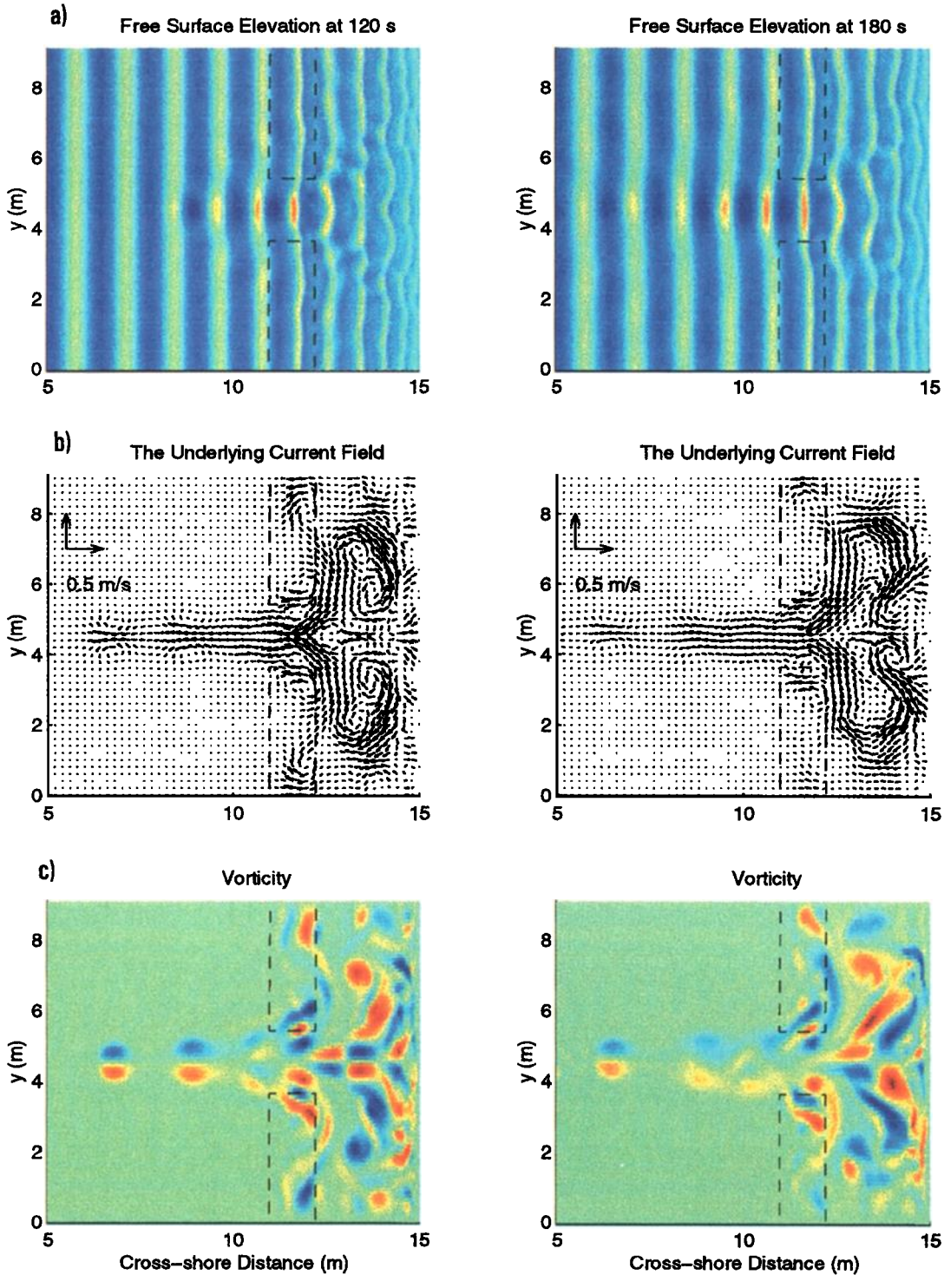

Plate 5. Computed (a) wave field, (b) underlying current, and (c) vorticity field at (left) t = 120 s and (right) t = 180 s.

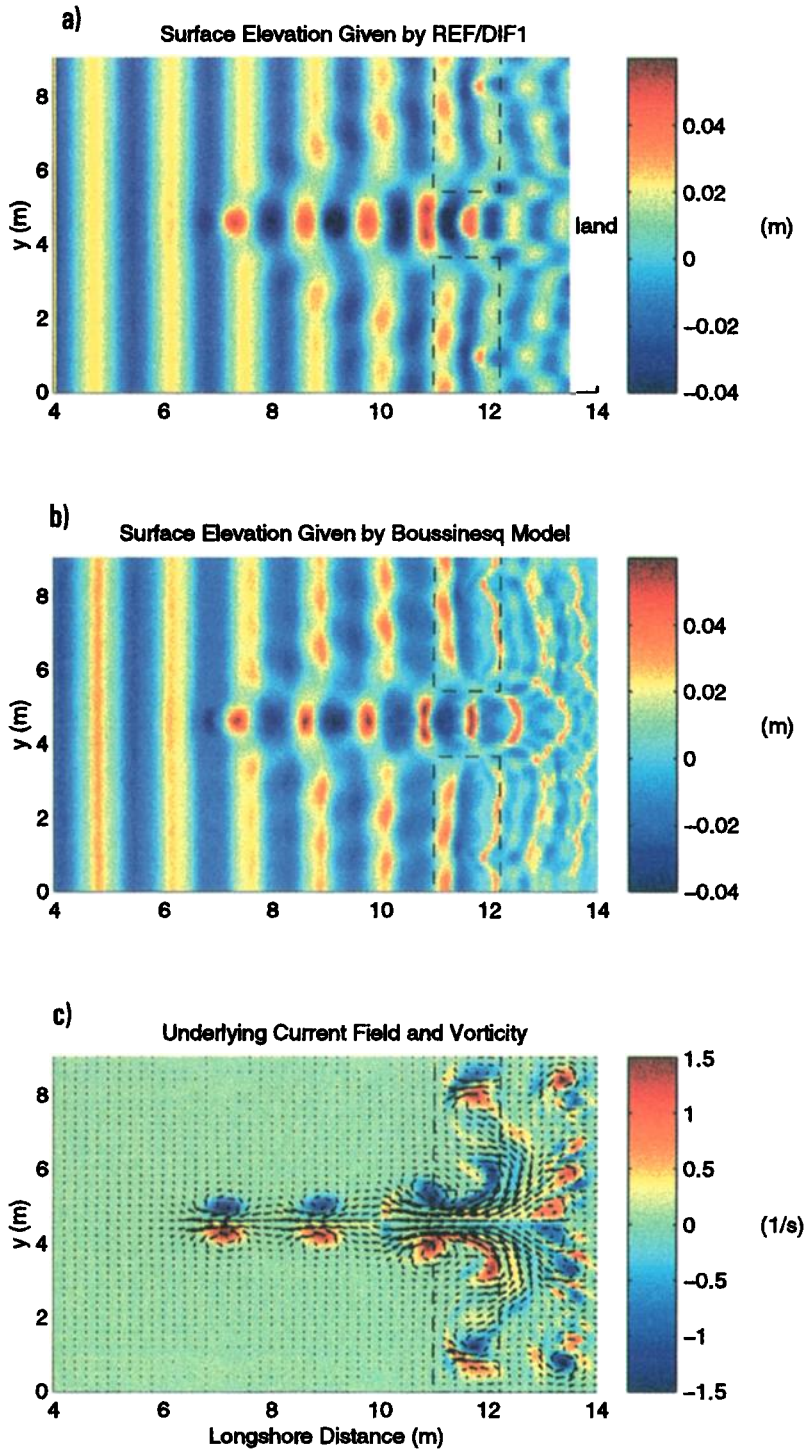

Plate 6. Wave refraction/diffraction by a rip current. (a) Surface elevation predicted by the REF/DIF model, (b) surface elevation predicted by the Boussinesq model, (c) underlying current field and vorticity.

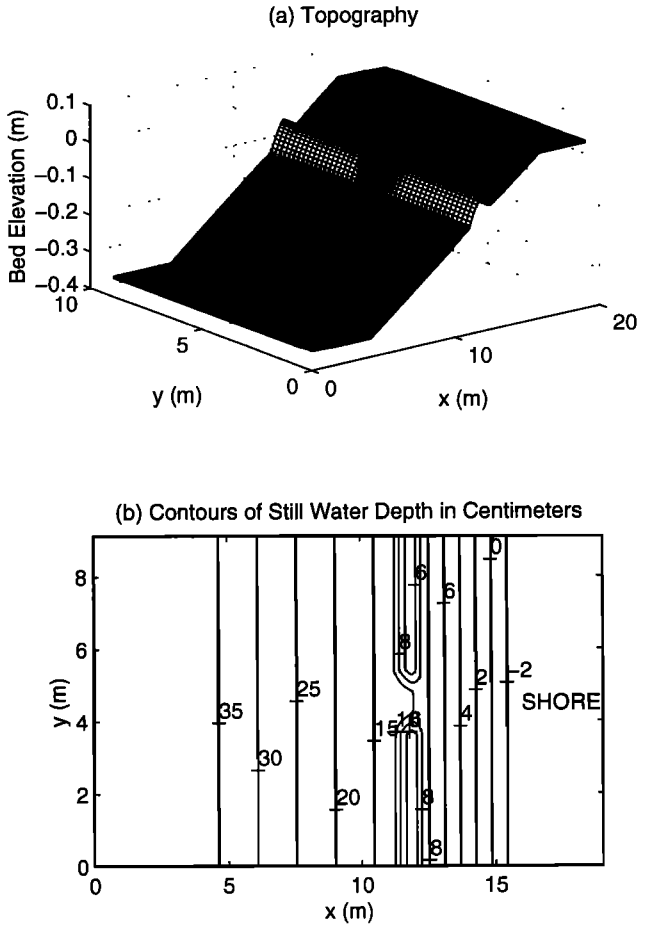

Figure 13. (a) Ideal topography and (b) contours of water depth.

the channel exit will be diminished after a longer simulation time owing to the rip oscillation. Consequently, the agreement between the modeled and measured wave heights in the rip channel is also expected to improve.

To establish a quantitative measure of model/data agreement, we use the index proposed by Wilmott [1981] as follows:

$$d = 1 - \frac{\sum_{j=1}^{n}[y(j) - x(j)]^2}{\sum_{j=1}^{n}[|y(j) - \bar{x}| + |x(j) - \bar{x}|]^2} \qquad (19)$$

where $x(j)$ are the measured data, $y(j)$ are the computed results from the numerical model, and $\bar{x}$ and $\bar{y}$ are the mean value of $x(j)$ and $y(j)$, respectively. When $d = 1$, it indicates a perfect agreement, while $d = 0$ means a completely disagreement. Table 1 lists the values of the index d for H_{rms}, mean water level $\bar{\eta}$, and cross-shore U and longshore V currents in the cases of experimental and ideal bathymetry. First, a comparison of the index for H_{rms} confirms that the experimental bathymetry gives better agreement of H_{rms} than does the ideal bathymetry. Second, with respect to $\bar{\eta}$, the numerical results agree well with the measurements in the case of experimental bathymetry, which is also better than the agreement of the ideal bathymetry. For cross-shore currents, the index in the case of using the survey bathymetric data is larger than that of ideal bathymetry with the same length of simulation time. In contrast, the ideal bathymetry leads to somewhat better agreement in terms of longshore current at $x = 12.3$ m.

In short, although small bathymetric perturbations may significantly alter the spatial and temporal variation of the rip current and the associated vortex structures, they may not substantially change the mean characteristics of the nearshore circulation in the sense of averaging over hundreds of waves.

5. Wave Refraction/Diffraction by Rip Currents

One of the advantages of the Boussinesq model is that wave-current interaction is automatically taken into account by the model. We have focused on the wave-induced currents in the previous sections. From the numerical results, we observe the significant effects of the underlying current on the surface wave transformation. One of the effects is wave refraction/diffraction by the vortices associated with the rip current.

In the literature, surface wave scattering by solid bodies, such as cylinders, has been well studied using the potential flow theory. However, gravity wave scattering by cylindrical fluid vortices has not drawn much attention. From a theoretical point of view, both scattering phenomena are different. When waves propagate in the inhomogeneous media owing to the presence of rip currents, combined wave diffraction and refraction will occur. In this section, we use the Boussinesq model and the REF/DIF model [*Kirby*, 1986] to examine the refraction/diffraction effects of a rip current on the surface wave field.

Given a current field by averaging the results of the Boussinesq model with the use of an ideal bathymetry, the REF/DIF model based on a parabolic approximation of the mild-slope equation [*Kirby and Dalrymple*, 1983] is used to compute the wave field with the combined refraction and diffraction. Plate 6 presents the wave field predicted by REF/DIF and the Boussinesq model with the underlying current field on the ideal topography. In comparison with the results of Boussinesq model as depicted by Plate 6b, REF/DIF gives a similar pattern of diffracted waves by the rip current accompanied with vortex pairs. The patches of hot colors on the wave crests illustrate the variation of the wave field in the longshore direction. Similar to the results given by the weakly nonlinear version of REF/DIF that incorporates the amplitude effect on the dispersion relation of a monochromatic wave, a linear version of REF/DIF also predicts the diffraction pattern. This indicates that the diffraction by the vortices is essentially a linear process.

Figure 18 gives a closer look at the cross-shore variation of free surface elevation along the center line of the rip channel, and Figure 19 illustrates the longshore nonuniformity of the wave height caused by the rip current. The dashed lines represent the Boussinesq results,

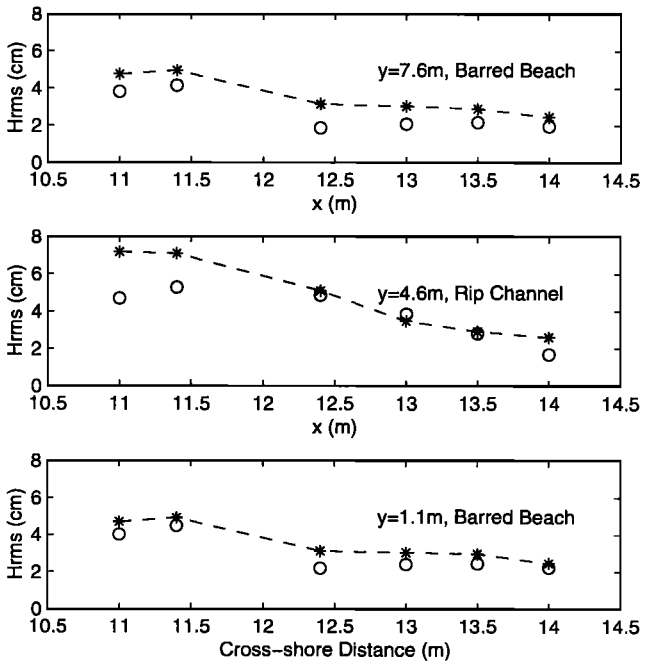

Figure 14. Comparison of computed (stars) and measured (circles) wave height in the case of ideal bathymetry.

while the solid lines are the REF/DIF results. Both models predict similar longshore nonuniformity of wave height owing to the diffraction by the rip accompanied with vortex pairs. The wave length of the diffracted waves in the longshore direction is comparable to the cross-shore wave length.

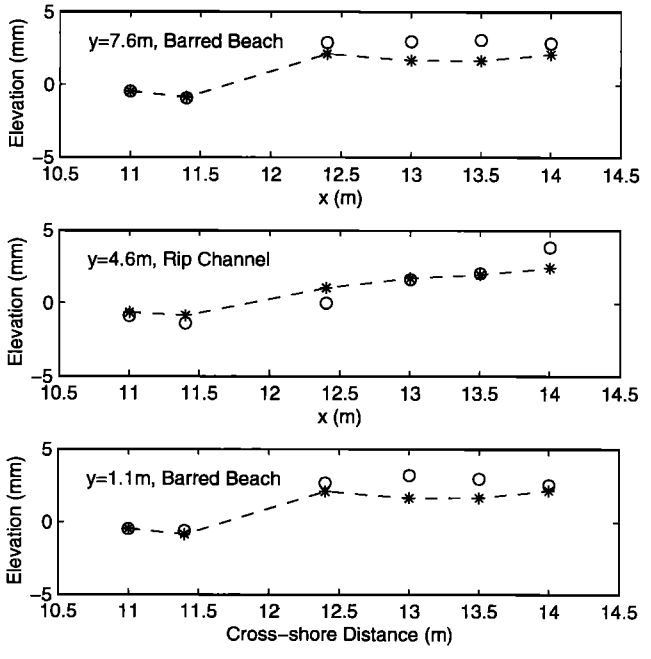

Figure 15. Comparison of computed (stars) and measured (circles) mean water level in the case of ideal bathymetry.

In the offshore area before $x = 8.0$ m, the free surfaces predicted by both models are in agreement because waves are essentially linear in that region. As expected, differences are observed when waves become more nonlinear because of the shoaling on the sloping beach. REF/DIF fails to predict the skewness and asymmetry of the shoaling waves. Weaker diffraction effects in the area far away from the vortices in the REF/DIF result compared with the Boussinesq model may be attributed to the parabolic approximation of REF/DIF. Nevertheless, the signature of longshore variation of wave height is captured by both models.

Because a jet-like rip current is unstable in nature [*Haller et al.*, 1997], any perturbations resulting from longshore nonuniformities of incoming waves and topography will lead to rip oscillation. The diffracted waves will cause nonuniformity of the radiation stresses in the longshore direction and may contribute to the complexity of the circulation pattern behind the submerged bar.

To illustrate the diffraction effect on vortex generation, Figure 20 shows the comparison of the longshore variation of the wave height and vorticity on the crest of the bar predicted by the Boussinesq model. Obviously, the variation of the wave height on the bar crest is coincident with the variation of the vorticity as the

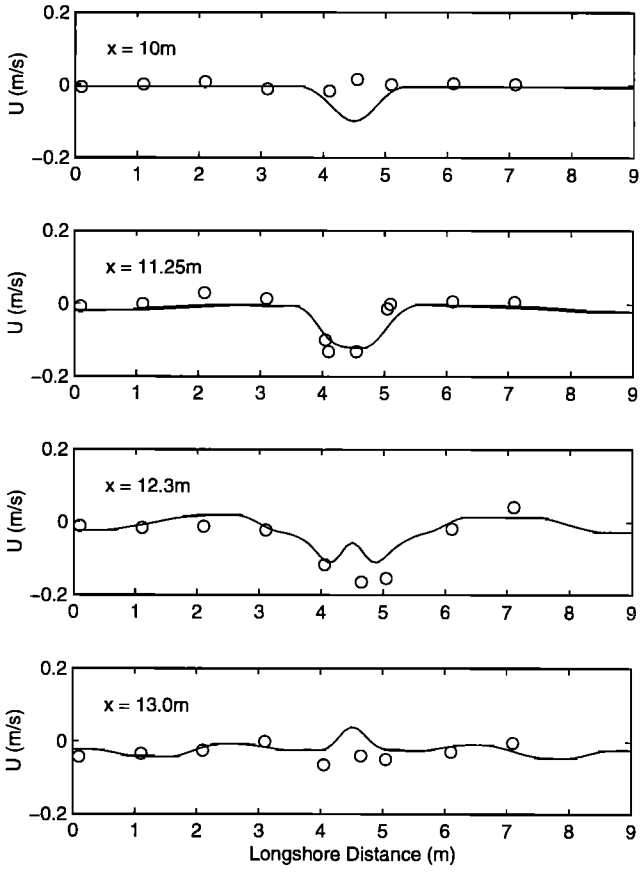

Figure 16. Comparison of computed (solid lines) and measured (circles) cross-shore mean velocity in the case of ideal bathymetry.

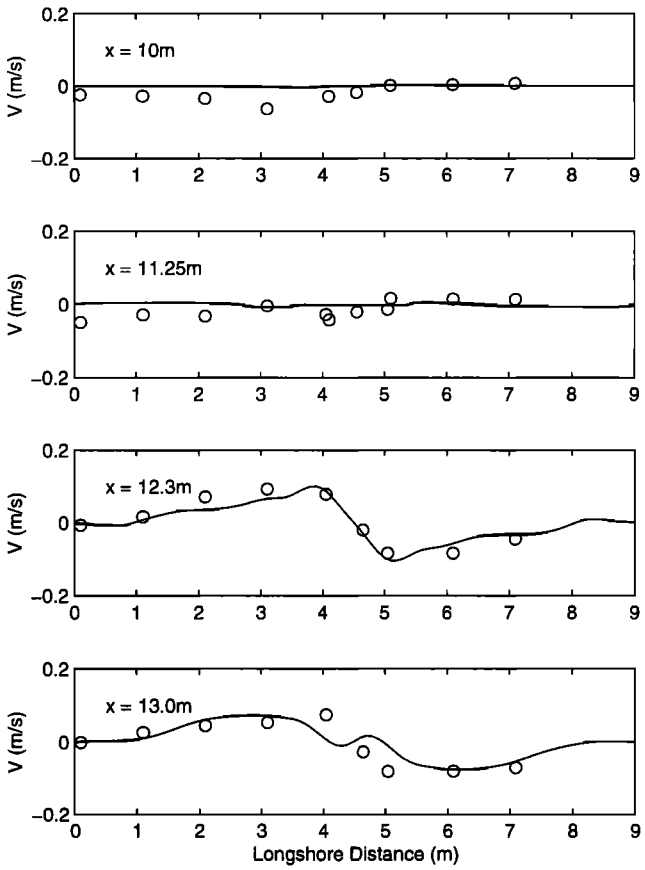

Figure 17. Comparison of computed (solid lines) and measured (circles) longshore mean velocity in the case of ideal bathymetry.

correlation coefficient is equal to 0.92 for both curves at $0 \leq x \leq 2.5$ m. Notice that the flow field is symmetric about the center line of the rip channel, while the vorticity field is antisymmetric. In addition, we also found that the wave length of the longshore variation is comparable to that of the cross-shore wave motion.

A comparison of Plates 1c and 4c, left, suggests that the bathymetric perturbations on the crest of the bar results in the production of vorticity there. We observe from an animation of the vorticity field that concentrated vorticity appears on the bar crest once vortex pairs in the rip channel are shed offshore in the case of ideal topography. The presence of vorticity on the submerged bar away from the rip channel is similar to

Table 1. Wilmott's [1981] Index as a Measure of Model/Data Agreement

Index	H_{rms}	$\bar{\eta}$	U	V	Bathymetry
d_1	0.97	0.98	0.92	0.85	experimental
d_2	0.85	0.92	0.82	0.92	ideal

Variables are defined as follows: H_{rms}, root-mean-square wave height; $\bar{\eta}$, mean water level; U, cross-shore current; and V, longshore current.

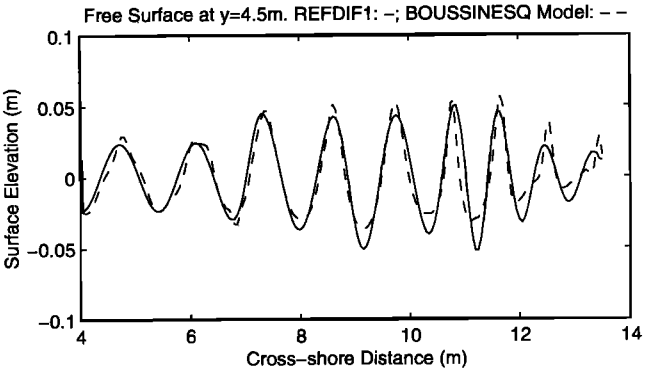

Figure 18. Comparison of the cross-shore variations of free surface predicted by the refraction/diffraction (REF/DIF) model (solid line) and the Boussinesq model (dashed line).

what we observed at the early stage of simulation before vortex shedding in the case of experimental topography with bathymetric perturbations on the bar crest (e.g., Plate 1c). Although the mechanism of vorticity generation in both cases is the longshore nonuniformity of breaking on the bar crest, the longshore variation of wave height in the case of ideal bathymetry is attributed to the diffraction effect of wave field by the rip current rather than the bathymetric perturbations.

The complex circulation pattern shoreward of the submerged bar results from the combined effects of the rip channel and wave refraction/diffraction by the rip current. Owing to the lack of small bathymetric perturbations in the case of ideal bathymetry, the influence of wave diffraction by the rip current is more profound because of the more organized vortex in comparison with those in section 3. However, in both cases of sections 3 and 4, the dominant mechanism of vorticity generation is the longshore nonuniformity of wave breaking owing to the presence of the rip channel.

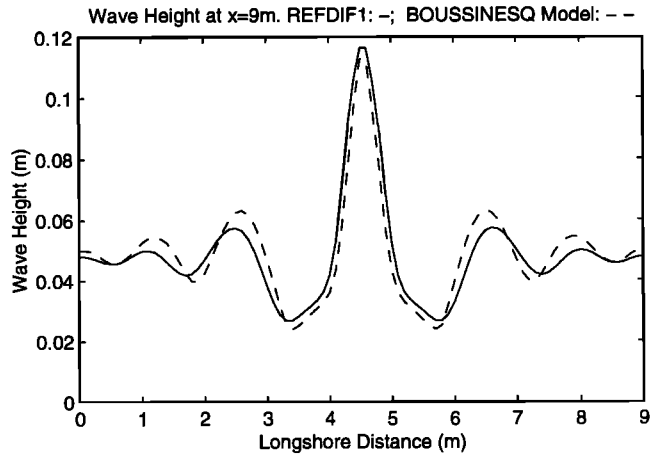

Figure 19. Comparison of the longshore variations of wave height predicted by the REF/DIF model (solid line) and the Boussinesq model (dashed line).

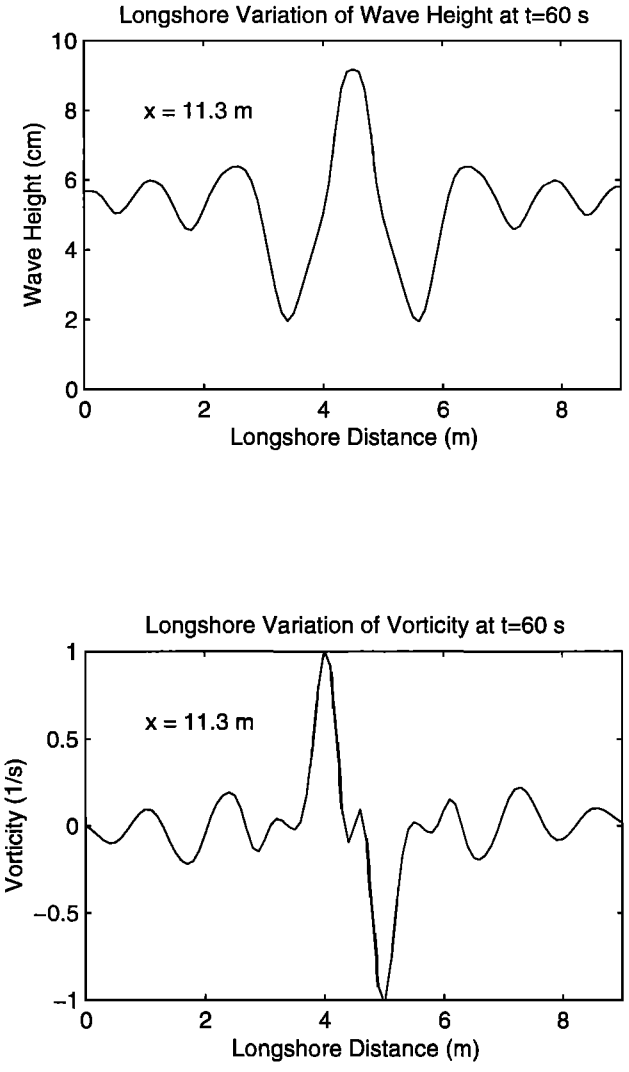

Figure 20. Longshore variations of (top) wave height and (bottom) vorticity near the bar crest.

6. Summary and Conclusions

A numerical model based on the fully nonlinear Boussinesq equations [*Wei et al.*, 1995] has been extended to include wave breaking and moving shorelines for simulation of wave transformation and wave-induced nearshore circulation. Fully coupled wave/current interaction is taken into account by the Boussinesq equations. The model not only predicts the nearshore propagation of nonlinear surface gravity waves but also gives the underlying unsteady flow generated by wave breaking. The current field is obtained by time averaging of the computed fluid particle velocity over two wave periods, while the vorticity field is computed directly from the instantaneous fluid particle velocities.

The model results are compared with the measurements from a laboratory experiment conducted by *Haller et al.* [1997] on rip current generation on a barred beach with rip channels. Fairly good agreement is observed between the laboratory data and the computed longshore and cross-shore currents, mean water level, and the root-mean-square wave height along several transects in the surf zone. The verified numerical model is employed to investigate the spatial and temporal variability of rip currents and associated vortices. The effect of bathymetric uniformity on rip instability and wave refraction/diffraction by the underlying rip current accompanied with vortex pairs are also studied.

In agreement with the physical experiment and theoretical prediction by *Haller et al.* [1997], the numerical results indicate that the rip current is unstable. The rip instability results in an oscillating rip current and the alongshore movement of vortices associated with the rip current.

It is found that the bathymetric uniformity of the barred beach in the longshore direction may delay the onset of instability and cause shedding of vortex pairs offshore. Although bathymetric perturbations can significantly alter the spatial and temporal variation of rip currents and vortex structures, they may not change the mean characteristics of the combined wave and current motion averaged over a long period of time, of the order of several hundred wave periods, because of the unstable nature of the rip current.

Wave diffraction by the rip current is observed from the numerical experiment. A parabolic model, REF/DIF [*Kirby*, 1986], for combined refaction and diffraction is also used to examine the effects of the vortices. The refracted/diffracted waves by the underlying current field cause nonuniformity of the radiation stresses in the longshore direction and may contribute to the complexity of the circulation pattern behind the submerged bar. Vorticity generation on the bar crest results from the longshore nonuniformity of breaking caused by either diffraction effects of the rip current or bathymetric perturbations. The numerical results obtained in this study are promising. Further verification of the observed phenomena in the numerical simulation by physical experiments is required.

Acknowledgments. This study has been supported by the Office of Naval Research, Base Enhancement Program and Coastal Dynamics Program, through research grants N00014-97-1-0283 and N00014-95-1-0075.

References

Birkemeier, W. A., and R. A. Dalrymple, Nearshore water circulation induced by wind and waves, paper presented at Symposium on Modeling Techniques, Am. Soc. of Civ. Eng., San Francisco, Calif., 1975.

Bowen, A. J., The generation of longshore currents on a plane beach, *J. Mar. Res., 73,* 2569-2577, 1969.

Carrier, G. F., and H. P. Greenspan, Water waves of finite amplitude on a sloping beach, *J. Fluid Mech., 4,* 97-109, 1958.

Chen, Q., P. A. Madsen, H. A. Schäffer, and D. R. Basco, Wave-current interaction based on an enhanced Boussinesq approach, *Coastal Eng., 33,* 11-40, 1998.

Chen, Q., J. T. Kirby, R. A. Dalrymple, A. B. Kennedy, and A. Chawla, Boussinesq modeling of wave transformation,

breaking, and run-up, II, 2D, *J. Waterw. Port Coastal Ocean Eng.*, in press, 1999.

Dalrymple, R. A., Rip currents and their causes, in *Proc. 16th Int. Conf. Coastal Eng.*, Reston, Va., Am. Soc. of Civ. Eng., 1414-1427, 1978.

Haller, M. C., R. A. Dalrymple, and I. A. Svendsen, Modeling rip currents and nearshore circulation, paper presented at Ocean Wave Measurement and Analysis, Am. Soc. of Civ. Eng., Virginia Beach, VA., 1997.

Karambas, T. V., and C. A. Koutitas, A breaking wave propagation model based on the Boussinesq equations, *Coastal Eng., 18,* 1-19, 1992.

Kennedy, A. B., Q. Chen, J. T. Kirby, and R. A. Dalrymple, Boussinesq modeling of wave transformation, breaking, and run-up, I, 1D, *J. Waterw. Port Coastal Ocean Eng.*, in press, 1999.

Kirby, J. T., Higher-order approximations in the parabolic equation method for water waves, *J. Geophys. Res., 91,* 933-952, 1986.

Kirby, J. T., Nonlinear, dispersive long waves in water of variable depth, in *Gravity Waves in Water of Finite Depth,* edited by J.N. Hunt, Computa. Mech. Publications, 55-126, 1997.

Kirby, J. T., and R. A. Dalrymple, A parabolic equation for the combined refraction-diffraction of Stokes waves by mildly varying topography, *J. Fluid Mech., 136,* 543-566, 1983.

Kobayashi, N., E. A. Karjadi, and B. D. Johnson, Dispersion effects on longshore currents in surf zones, *J. Waterw. Port Coastal Ocean Eng., 123,* 240-248, 1997.

Liu, P. L.-F., Y.-S. Cho, M. J. Briggs, U. Kanoglu, and C. E. Synolakis, Runup of solitary waves on a circular island, *J. Fluid Mech., 302,* 259-285, 1995.

Longuet-Higgins, M. S., Longshore currents generated by obliquely incident sea waves, 1, *J. Geophys. Res., 75,* 6778-6789, 1970a.

Longuet-Higgins, M. S., Longshore currents generated by obliquely incident sea waves, 2, *J. Geophys. Res., 75,* 6790-6801, 1970b.

Longuet-Higgins, M. S., and R. W. Stewart, The changes in amplitude of short gravity waves on steady non-uniform currents, *J. Fluid Mech., 10,* 529-549, 1961.

Madsen, P. A., and O. R. Sørensen, A new form of the Boussinesq equations with improved linear dispersion characteristics, 2, A slowly varying bathymetry, *Coastal Eng., 18,* 183-204, 1992.

Madsen, P. A., and H. A. Schäffer, A review of Boussinesq-type equations for gravity waves, in *Advances in Coastal and Ocean Engineering,* edited by P. L.-F. Liu, World Scientific, River Edge, NJ, in press, 1999.

Madsen, P. A., O. R. Sørensen, and H. A. Schäffer, Surf zone dynamics simulated by a Boussinesq-type model, I, Model description and cross-shore motion of regular waves, *Coastal Eng., 32,* 255-287, 1997.

Nwogu, O., Alternative form of Boussinesq equations for nearshore wave propagation, *J. Waterw. Port Coastal Ocean Eng., 119,* 618-638, 1993.

Peregrine, D. H., Surf zone currents, *Theoret. Comput. Fluid Dyn., 10,* 295-309, 1998.

Schäffer, H. A., P. A. Madsen, and R. A. Deigaard, A Boussinesq model for waves breaking in shallow water, *Coastal Eng., 20,* 185-202, 1993.

Smagorinsky, J., S. Manabe, and J. L. Holloway, Numerical results from a nine-level general circulation model of the atmosphere, *Mon. Weather Rev., 93,* 727-768, 1965.

Svendsen, I. A., and U. Putrevu, Surf-zone hydrodynamics, in *Advances in Coastal and Ocean Engineering, Vol. 2,* edited by P.L.-F. Liu, World Scientific, River Edge, NJ, pp. 1-78, 1995.

Svendsen, I. A., K. Yu, and J. Veeramony, A Boussinesq breaking wave model with vorticity, in *Proc. 25th Int. Conf. Coastal Eng.*, Reston, Va., Am. Soc. of Civ. Eng., 1192-1204, 1996.

Tao, J., Numerical modeling of wave run-up and breaking on the beach (in Chinese), *Acta Oceanol. Sin., 6,* 692-700, 1984.

Wei, G., Simulation of water waves by Boussinesq models, Ph.D. thesis, 202 pp., Dep. of Civ. Eng., Univ. of Delaware, Newark, 1997.

Wei, G., J. T. Kirby, S. T. Grilli, and R. Subramanya, A fully nonlinear Boussinesq model for surface waves, 1, Highly nonlinear unsteady waves, *J. Fluid Mech., 294,* 71-92, 1995.

Wei, G., J. T. Kirby, and A. Sinha, Generation of waves in Boussinesq models using a source function method, *Coastal Eng., 36,* 271-299, 1999.

Wilmott, C. J., On the validation of models, *Phys. Geogr., 2,* 219-232.

Zelt, J. A., The run-up of nonbreaking and breaking solitary waves, *Coastal Eng., 15,* 205-246, 1991.

Q. Chen, R. A. Dalrymple, M. C. Haller, A. B. Kennedy, and J. T. Kirby, Center for Applied Coastal Research, University of Delaware, Newark, DE 19716. (e-mail: qchen@coastal.udel.edu; rad@coastal.udel.edu; merrick@coastal.udel.edu; kennedy@coastal.udel.edu; kirby@coastal.udel.edu)

(Received June 23, 1998; revised March 9, 1999; accepted March 24, 1999.)